

國立交通大學

應用化學系

碩士論文

三維雷利散射顯微術及成像於活體葉綠體中基粒之研究

Three-dimensional Rayleigh Scattering Microspectroscopy
and Imaging of *in vivo* Single Grana inside Chloroplast

研究生：黃鈴婷 (Ling-Ting Huang)

指導教授：增原宏 教授 (Prof. Hiroshi Masuhara)

中華民國一百零一年七月

三維雷利散射顯微術及成像於活體葉綠體中基粒之研究

**Three-dimensional Rayleigh Scattering Microspectroscopy
and Imaging of *in vivo* Single Grana inside Chloroplast**

研究生：黃鈴婷

Student: Ling-Ting Huang

指導教授：增原宏 博士

Advisor: Dr. Hiroshi Masuhara

國立交通大學
應用化學系碩士班
碩士論文



A Thesis
Submitted to M. S. Program
Department of Applied Chemistry
National Chiao Tung University
in partial Fulfillment of the Requirements
for the Degree of
Master
in
Applied Chemistry

July 2012

Hsinchu, Taiwan, Republic of China

中華民國一百零一年七月

三維雷利散射顯微術及成像於活體葉綠體中基粒之研究


研究生：黃鈴婷

指導教授：增原宏 博士

國立交通大學

應用化學系碩士班

摘要

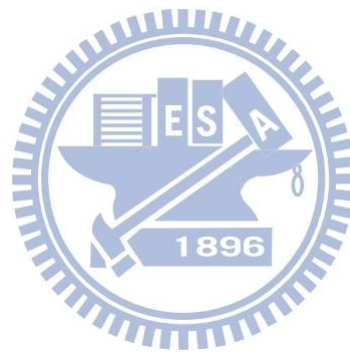


在此研究中，我們著重於雷利散射共聚焦顯微術及成像系統的應用，尤其在亞微米及奈米粒子的觀測。基粒（Grana）為數個盤狀的類囊體堆疊形成亞微米的大小而散布於葉綠體裡，故可視為行光合作用的最小單位。基粒的大小與其化學組成被認為具有不均質性，從這觀點出發，結合顯微影像及光譜的量測有助於分子的辨別並討論基粒的大小與光合作用的關係。

從水蘊草細胞的共聚焦影像中，我們可以清楚的觀察到基粒隨機地在葉綠體裡頭分布。量測單一基粒的光散射光譜時，我們察覺每一個基粒的光譜都不完全相同，並且觀察到基粒的位置（在葉綠體的中間或外圍，或是葉綠體坐落在葉子裡的任一位置）不影響光譜的量測結果。最重要的發現是基粒的尺寸相關性：當基粒的尺寸越大時，其波長

會往紅外線區移動。此外，我們還用極化光測基粒的特性，證實它是光學各向異性 (optical anisotropy)。根據分析結果我們推測：在較大的基粒裡存有較多的葉綠素分子，此外，在雷射照射下，尺寸大的基粒裡分子排列得愈發整齊，這也暗示了基粒光合作用的效率與它的尺寸大小有關。

為證實實驗數據的可信度，我們製備了含有金奈米粒子的晶體，並且成功地測得金奈米粒子的光散射光譜，即便它非常小又存在於晶體之中。另一方面，此實驗亦證實了我們系統的優異性能。



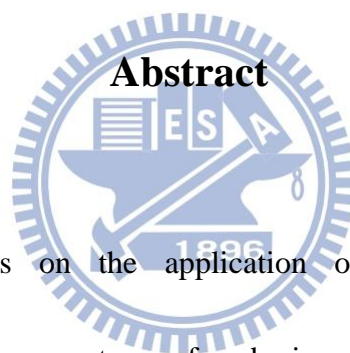
Three-dimensional Rayleigh Scattering Microspectroscopy and Imaging of *in vivo* Single Grana inside Chloroplast

Student: Ling-Ting Huang

Advisor: Prof. Hiroshi Masuhara

M. S. Program, Department of Applied Chemistry

National Chiao Tung University



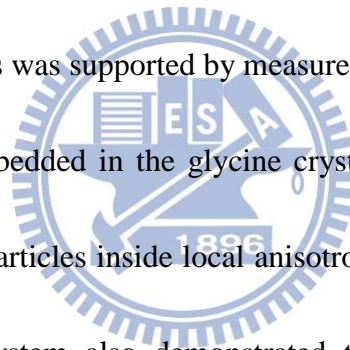
Abstract

In this study, we focus on the application of confocal Rayleigh scattering microspectroscopic and imaging system of submicron- to nanometer-sized particles, especially *in vivo* biological substances. In chloroplast of plant cell, submicrometer-sized grana are widely arranged and play a role of light-harvesting. The size and chemical composition of grana are considered to possess inhomogeneity. With this viewpoint, combining confocal microscopic imaging with spectroscopic measurement helps us to identify the molecules and to discuss the function of the grana in terms of their sizes.

Confocal images of chloroplasts of *Egaria densa* depicted the spatial distribution of

grana. The light scattering spectra of the grana depend on the granum size, although the spectra are independent on the position of the granum, in the center or on the exterior of the chloroplast. The greatest finding is that the spectrum is red-shifted as the granum size enlarges. Polarization measurement indicated that grana are optically anisotropic. According to our analyses, the obtained result suggested that there are more chlorophyll pigments in larger granum and the molecules align much better in larger ones when irradiated by laser. Based on the inference, we suppose that the light-harvesting property of grana is reflected in size.

The reliability of the results was supported by measurement of the light scattering spectra of 40 nm Au nanoparticles embedded in the glycine crystal, which can be considered as a model system containing nanoparticles inside local anisotropic surrounding, similar to that in the chloroplast. This model system also demonstrated that confocal Rayleigh scattering microspectroscopic and imaging system is a powerful tool for detection of single nanoparticles.



Acknowledgement

Firstly, I would like to sincerely appreciate Prof. Hiroshi Masuhara (Department of Applied Chemistry and Institute of Molecular Science, National Chiao Tung University) for supervising my research studies during these two years. I am very happy to meet him and become one of the members in his team. Prof. Masuhara is very nice and shares his unique opinions to not only work but life. I really learned a lot from his thinking process.

I am truly grateful to Prof. Takayuki Uwada (Department of Chemistry, Josai University, Japan) for his instruction. Prof. Uwada is very interesting and gives me lots of help in experiment. Though he is now in Japan and very busy, he is still concerned about me. I am glad to be his student from the bottom of my heart.

I would like to express my gratitude to Dr. Anwar Usman (Department of Applied Chemistry and Institute of Molecular Science, National Chiao Tung University) for correcting my master thesis and sharing his thoughts of Germany.

Besides, I want to thank Prof. Atushi Miura, Dr. Ken-ichi Yuyama (Department of Applied Chemistry and Institute of Molecular Science, National Chiao Tung University) and Prof. Teruki Sugiyama (Instrument Technology Research Center, National Applied Research

Laboratories). Prof. Miura takes care of all of the affairs in the laboratory. Dr. Yuyama and I had some discussion and that improve my understanding of study. Prof. Sugiyama gave specific comments and suggestions that helped me a lot in experiment.

Many thanks to all the members inclusive of Ms. Wen-Yu Lee, Mr. Ping-Yu Hee, Ms. Jing-Ru Tu, Mr. Tsung-Han Liu, Mr. Chong-Wei Huang and my classmates including Mr. Shung-Fa Wang, Mr. Tsu-Wei Hsu, Mr. Wei-Yi Chiang, Mr. Yan-Hua Huang, Mr. Ching-Shie Tseng and Mr. Chi-Shiun Wu. They helped me a lot not only for research but also daily life. I certainly wish them will get great achievement in the future.

Finally, I am greatly indebted to my family for their mentally concern and support to finish my study.



Table of Contents

| | |
|--|----|
| Chapter 1 Introduction | 1 |
| 1.1 Confocal microspectroscopy | 1 |
| 1.1-1 History of microscopy | 1 |
| 1.1-2 Light scattering and absorption microscopy to evaluate electronic structure | 1 |
| 1.1-3 Confocal microscopy using supercontinuum | 2 |
| 1.1-4 Confocal light scattering using supercontinuum | 4 |
| 1.2 Motivation for microspectroscopic study of complex nanostructure | 5 |
| 1.2-1 Plant cell | 5 |
| 1.2-2 Metal-organic hybrid material | 9 |
| Chapter 2 Principle | 10 |
| 2.1 Optical properties of particles | 10 |
| 2.1-1 Mie theory | 10 |
| 2.1-2 Rayleigh scattering | 16 |
| 2.1-3 Refractive index of metallic and organic nanoparticles | 18 |
| Chapter 3 Experimental setup | 20 |
| 3.1 Light source | 20 |
| 3.2 Confocal Rayleigh scattering microspectroscopic imaging system | 23 |
| 3.3 Experimental setup for crystallization | 24 |
| Chapter 4 Three dimensional morphological and spectroscopic study of <i>Egeria densa</i> .. | 27 |
| 4.1 Sample preparation | 28 |
| 4.2 Results and discussion | 30 |
| 4.2-1 Three dimensional morphological analysis of <i>Egeria densa</i> | 30 |

| | |
|---|-----------|
| 4.2-2 Confocal light scattering microspectroscopic analysis of grana in <i>Egeria densa</i> ... | 36 |
| 4.3 Discussion..... | 51 |
| 4.4 Summary..... | 56 |
| Chapter 5 Three dimensional spectroscopic characterizations of glycine crystals incorporated with Au NPs | 58 |
| 5.1 Sample preparation | 58 |
| 5.2 Results..... | 61 |
| 5.3 Summary | 68 |
| Chapter 6 Conclusion..... | 69 |
| Reference..... | 71 |



Lists of Figures

Chapter 1 Introduction

| | |
|--|---|
| Figure 1.1 Schematic illustration of sunlight collection..... | 7 |
| Figure 1.2 Chlorophyll pigments in the LHC-II trimer and monomer..... | 7 |
| Figure 1.3 Molecular structure of typical chlorophyll pigment..... | 8 |
| Figure 1.4 Electron micrographs of plant cell. (a) chloroplast (b) granum..... | 8 |

Chapter 2 Principle

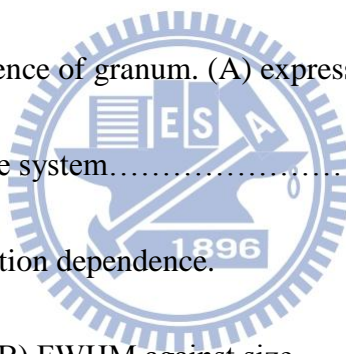
| | |
|--|----|
| Figure 2.1 Spherical polar coordinate system centered on a spherical particle..... | 12 |
| Figure 2.2 Light scattering, absorption, and extinction by a single particle..... | 13 |
| Figure 2.3 Calculated spectra of 100 nm Au nanoparticles with various refractive indices.... | 19 |

Chapter 3 Experimental setup

| | |
|--|----|
| Figure 3.1 Picture of mode-locked Ti: sapphire laser, Tsunami..... | 21 |
| Figure 3.2 The mode-locking principle of Tsunami..... | 21 |
| Figure 3.3 Picture of supercontinuum..... | 22 |
| Figure 3.4 The light scattering spectrum of supercontinuum..... | 22 |
| Figure 3.5 Schematic illustration of confocal Rayleigh scattering microspectroscopic and | |

| | |
|--|----|
| imaging system..... | 23 |
| Figure 3.6 Laser light source and microscopic system for crystallization..... | 26 |
| Figure 3.7 Picture of inverted microscope and other accessories..... | 26 |
| | |
| Chapter 4 Three dimensional morphological and spectroscopic study of <i>Egeria densa</i> | |
| Figure 4.1 Photograph of <i>Egeria densa</i> in the aquarium..... | 28 |
| Figure 4.2 Sample of <i>Egeria densa</i> | 29 |
| Figure 4.3 (A) Bright field and (B) Dark field image of plant cell of <i>Egeria densa</i> | 30 |
| Figure 4.4 Light scattering image of plant cell without zooming in..... | 32 |
| Figure 4.5 Light scattering image of plant cell with three times zoom..... | 32 |
| Figure 4.6 Light scattering image of plant cell with ten times zoom..... | 33 |
| Figure 4.7 Light scattering images of a living plant cell at different depth..... | 33 |
| Figure 4.8 Line profile method. (A) The chloroplast image. (B) Gaussian curve to fit the distribution..... | 35 |
| Figure 4.9 The definitions of small and large grana..... | 35 |
| Figure 4.10 The statistic chart of size distribution of grana..... | 36 |
| Figure 4.11 The light scattering spectrum of granum..... | 37 |
| Figure 4.12 Light scattering image and spectra of grana. (A) Light scattering images of chloroplasts. (B) The corresponding spectra of grana..... | 38 |

| | |
|---|----|
| Figure 4.13 Light scattering spectra of grana. (A) Single Soret band (B) Soret band with a shoulder (C) Soret band with split peaks..... | 38 |
| Figure 4.14 Correlation of the peak wavelength of the Soret band against size..... | 39 |
| Figure 4.15 Light scattering image and spectra of grana. (A) confocal image (B) spectra of grana inside the chloroplast (C) spectra of grana surfacing the chloroplast..... | 40 |
| Figure 4.16 Schematic illustration of polarization measurement..... | 40 |
| Figure 4.17 The polarization measurement of 200 nm Au nanoparticle..... | 44 |
| Figure 4.18 Scattering spectra of granum with various polarizations..... | 44 |
| Figure 4.19 Polarization dependence of granum. (A) expressed in Cartesian coordinate system (B) Polar coordinate system..... | 45 |
| Figure 4.20 Analyses of polarization dependence. (A) R against size (B) FWHM against size..... | 46 |
| Figure 4.21 Fluorescent images and spectra. The fluorescent images of plant cell (A) without magnification and (B) with ten times zoom. The fluorescent spectra of grana (C) within same chloroplast and (D) in different chloroplasts..... | 49 |
| Figure 4.22 The analysis of size dependence..... | 51 |
| Figure 4.23 The calculation of chlorophyll <i>a</i> nanoparticles..... | 55 |
| Figure 4.24 The plot of peak wavelength of the Soret band against size..... | 56 |



Chapter 5 Three dimensional spectroscopic characterizations of glycine crystals incorporated with Au NPs

Figure 5.1 Picture of laser focusing at air/solution interface.....60

Figure 5.2 Picture of laser-induced crystals.....60

Figure 5.3 Picture of sample of glycine crystals.....60

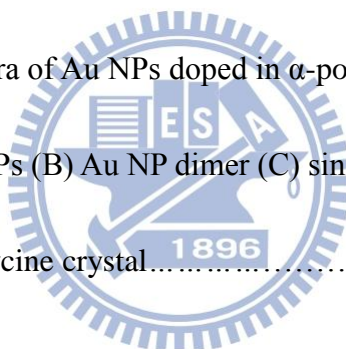
Figure 5.4 The pictures of glycine crystal incorporated Au NPs.....64

Figure 5.5 The tomography of glycine crystal.....65

Figure 5.6 The picture of glycine crystal corresponding to the confocal image.....65

Figure 5.7 Light scattering spectra of Au NPs doped in α -polymorph glycine crystal.
(A) aggregated Au NPs (B) Au NP dimer (C) single Au NP.....66

Figure 5.8 Pictures of γ -form glycine crystal.....67



Chapter 1 Introduction

1.1 Confocal microspectroscopy

1.1-1 History of microscopy

Microscopy has been widely used and there has been a great effort to improve the resolution and precision. Electron microscopy, in particular, can detect very small objects down to a few nanometers, but the cost is high and the convenience is relative low. Optical microscopy, though its spatial resolution is usually determined by diffraction limit of light, now becomes essential tool for characterization of nanostructures. Advances in digital imaging and analysis have also enabled microscopists to acquire quantitative measurements quickly and efficiently [1]. With the help of techniques, such as dark-field, phase contrast, fluorescence, and confocal, the specimen contrast is improved. The following sections would give further discussions.

1.1-2 Light scattering and absorption microscopy to evaluate electronic structure

To identify the electronic structure of molecules, absorption spectroscopy is usually the first choice because of the specificity and the quantitative character. However, for

nanoparticles (NPs), it is hard to measure the absorption spectra and to distinguish each one based upon Lambert-Beer Law; the short path length limits the interaction between the illumination light and the NPs, also the illumination beam is too large compared to their sizes resulting from the diffraction limit of light.

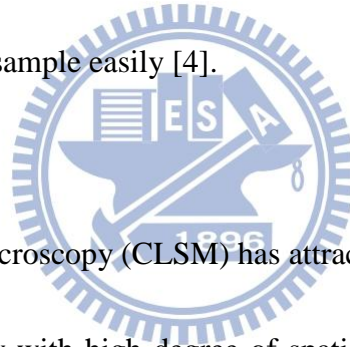
Recently, photothermal microspectroscopy is developed to measure single noble metallic NPs, based on the change of refractive index due to changes in temperature and density of the sample [2]. Furthermore, Photothermal Heterodyne Imaging (PHI) allows for the unprecedented detection of gold NPs down to 1.4 nm in diameter [3]. Because heating is necessary for PHI technique, it is not suitable for nonmetallic objects. On the other hand, light scattering microspectroscopy can be applied to not only nonfluorescent but also nonmetallic NPs. Combining dark-field technique which detects only scattered light from sample performs high contrast and S/N ratio by black background. From a viewpoint of electronic information, scattering relies on the same basic optical response to the absorption process, so the scattering spectroscopy is an alternative measurement to evaluate the electronic structure.

1.1-3 Confocal microscopy using supercontinuum

Confocal microscopy has been developed to be a powerful tool for a few decades for the high contrast and single-point measurement. Especially, the combination of the visualization

of 3-D structure and spectra improves the application in biological and medical science.

Point light source illuminates at the focal plane, detecting object in a point, so that the light source and the detected spot are confocal. The pointed detection then is imaged at the pinhole. Confocal microscopy is originated in three mutually confocal points and the key technique is the spatial filter. With an aperture, the out-of-focus light would be blocked and permits only the well-defined point forming image, hence the contrast is increased. Furthermore, scanning with a pair of mirrors (Galvano mirror) constructs the three-dimensional image of the sample easily [4].



Confocal laser scanning microscopy (CLSM) has attracted much more attentions because laser shows high energy density with high degree of spatial and temporal coherence, which increases the resolution and signal intensity. W. Denk *et al* succeeded in two-photon laser scanning fluorescent measurement by CLSM [5]. With a colliding-pulse-mode-locked (CPM) dye laser producing ultrashort pulses, the probability of two-photon molecular excitation becomes appreciable [5]. Brakenhoff *et al.* demonstrated that the section inherent to two-photon imaging could be improved by the introduction of confocal aperture with amplified Ti: Sapphire laser [6]. The use of femtosecond laser can shield sample from heat generation and damage; however, the tuning range is limited and the available excitation

range does not efficiently excite fluorophores designed for single-photon excitation [7].

Supercontinuum is the formation of spectra broadening by an intense laser propagating through a nonlinear media. The characteristics of supercontinuum are the huge bandwidth, spatial coherence, and high brightness. The huge bandwidth provides a broad range of spectroscopic transitions in which many species can be detected simultaneously. The high spectral brightness and spatial coherence give high spectral resolutions [8].

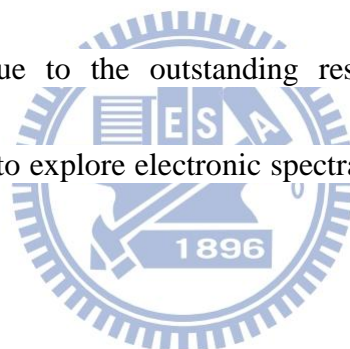
Stefano and his coworker presented a new approach of reflectance laser scanning confocal system in which the spectroscopic imaging capabilities are achieved with the help of wavelength-tunable source [9]. The use of supercontinuum confocal microscope in combination with fluorescence for spectrally resolved imaging offers a great analysis of the details of living cells [10].

1.1-4 Confocal light scattering using supercontinuum

CLSM combined with fluorescence has been widely used for the study of living tissue, especially in imaging [11]. The application of confocal imaging and fluorescence correlation spectroscopy (FCS) to characterize well-defined lipid bilayer models was reported two decades ago [12]. However, fluorescence spectroscopy is limited to fluorescent materials,

quenching, and environmental factors, which have to be controlled during the analyses to obtain the reproducible measurements [13].

Scattering, on the other hand, is free from the limitations of fluorescence. Additionally, combining confocal system and supercontinuum give an effective technique for nanostructure. Lindfors *et al.* have demonstrated that confocal microscopy using supercontinuum reveals spectroscopy and imaging of single Au NPs down to 10 nm [14]. Since noble metallic NPs exhibit strong scattering in visible region, it recently has been developed as label-free plasmonic biosensors [15]. Due to the outstanding results obtained by confocal light scattering [14, 15], we are able to explore electronic spectral properties of nanostructure with a high spatial resolution.



1.2 Motivation for microspectroscopic study of complex nanostructure

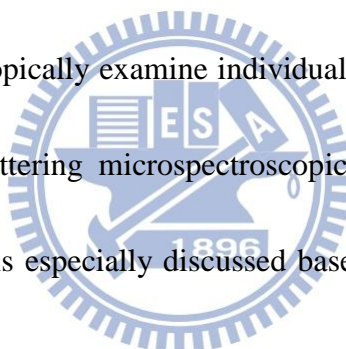
1.2-1 Plant cell

Sunlight collection and the subsequent energy transfer are included in the process of photosynthesis (Fig. 1.1). A photosystem contains a reaction center associated with numbers of light-harvesting complexes (LHC) composed of proteins where chlorophyll pigments embedded (Fig. 1.2). Chlorophyll pigments (Fig. 1.3) absorb photons and then start a flow of electron transport within LHC to the reaction center. Reaction center also contains a complex

of proteins and pigments, which controls the chemical reactions during photosynthesis.

Photosystems are bound to dicoidal thylakoid membranes forming stacked thylakoids, granum (Fig. 1.4), and the stroma lamellae which are unstacked thylakoids and connect grana [16]. The stacked thylakoids are considered to possess high energy transfer efficiency so that grana can be regarded as heterogeneous photo-chemical reaction center in nature, and the study of the inhomogeneity will make the function clear.

In this study, we spectroscopically examine individual grana as a function of the size by utilizing confocal Rayleigh scattering microspectroscopic imaging system. The molecular arrangement in thylakoid units is especially discussed based on the polarization dependence of scattering spectrum of granum.



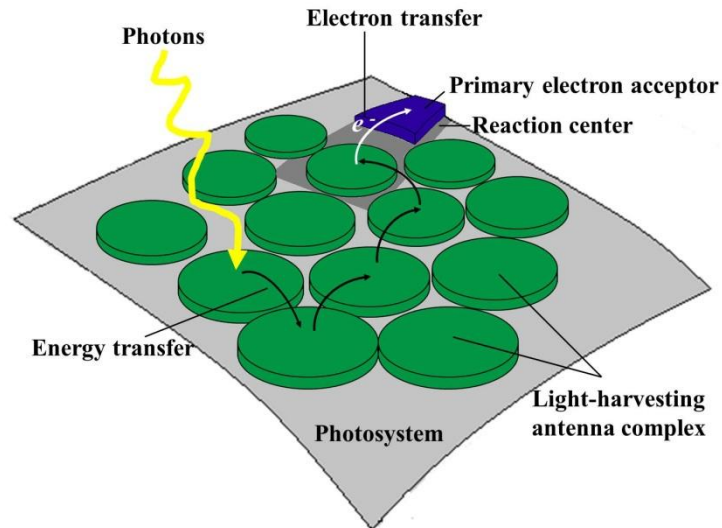


Figure 1.1 Schematic illustration of sunlight collection. Photons are captured in the light-harvesting antenna complex by chlorophyll and other accessory pigments. When sufficient energy is obtained, an electron is transferred to the reaction center to proceed photosynthesis.

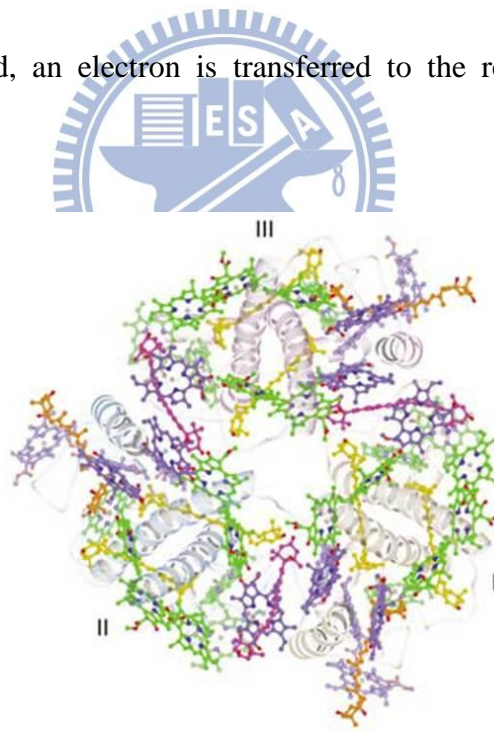


Figure 1.2 Pigments in the LHC-II trimer and monomer. Stereo view shows the pigment arrangement pattern in the LHC-II trimer. Monomers are labeled I–III. For clarity, the chlorophyll phytol chains and lipids are omitted. Green, Chl *a*; blue, Chl *b*; yellow, lutein; orange, neoxanthin; magenta, xanthophyll-cycle carotenoids [17].

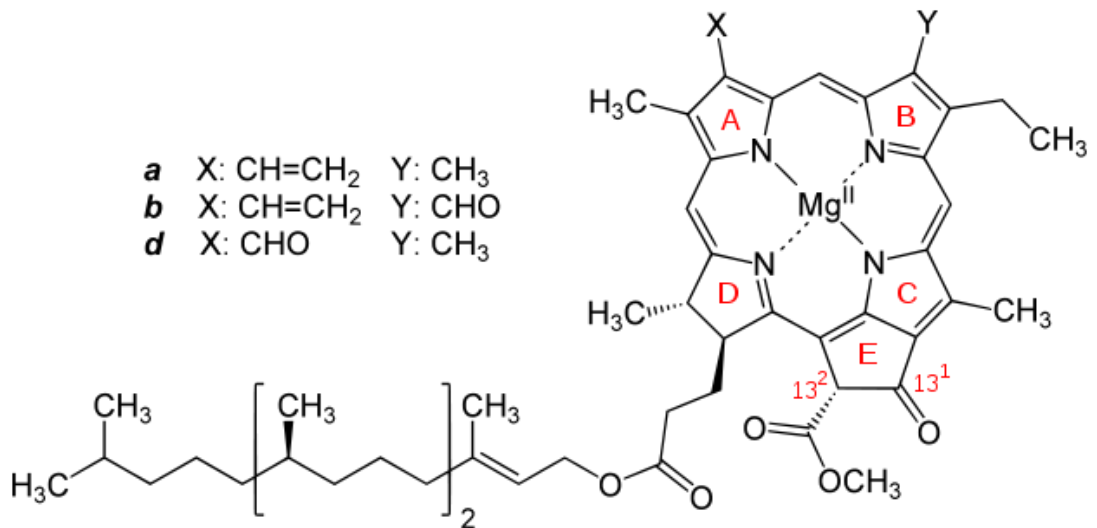


Figure 1.3 A typical chlorophyll molecule contains a porphyrin and a long phytol chain.

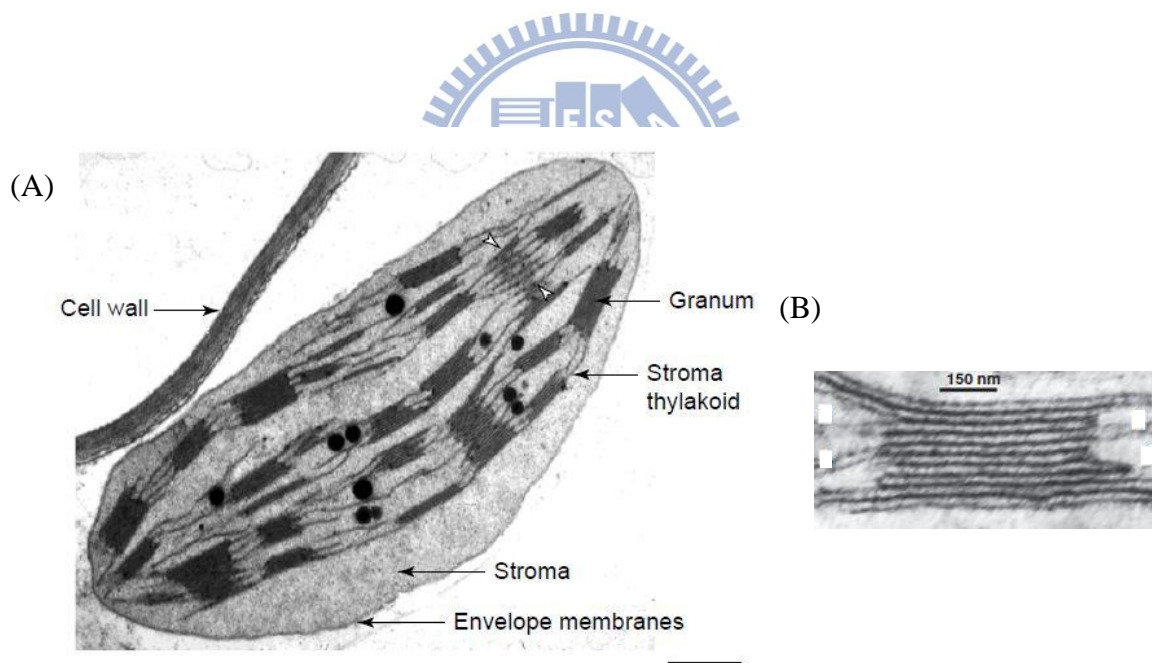
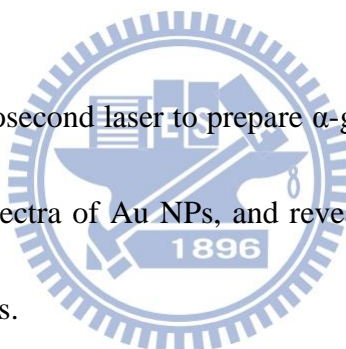


Figure 1.4 (A) Thin-section electron micrograph of a higher plant chloroplast. Stroma thylakoids can be seen in a tilted position between two white arrowheads. Scale bar = 0.5 mm [18]. (B) Tomographic section of isolated thylakoid membranes, granum [19].

1.2-2 Metal-organic hybrid material

Grana are submicron-sized particles inside the natural complex system. To ensure the reliability of the measurement of grana, we prepare another sample; i.e. Au NPs embedded inside glycine crystal which is the artificial complex system as a model system containing NPs in anisotropic surrounding. By measuring the scattering spectra of Au NPs, which can be corrected by computational calculation, we also show the advantages of confocal Rayleigh scattering microspectroscopy and imaging system.

In this work, we used femtosecond laser to prepare α -glycine crystal fabricating with Au NPs, measured the scattering spectra of Au NPs, and revealed the spatial distribution of Au NPs by three-dimensional images.



Chapter 2 Principle

When a particle is irradiated by electromagnetic waves, electrons perform oscillated motion with the electric field of the incident wave. Electric charges accelerated by the incident wave radiate electromagnetic energy in all directions.

Modes of light scattering can be divided into three domains according to the size of particle. If the particle size is much smaller compared to the wavelength of light, it is called Rayleigh scattering; if the size is about the wavelength of light, it is called Mie scattering, and if the size is larger than the wavelength of light, it is called geometric scattering. In this study, as the wavelength of light are within the visible to near infrared, Rayleigh and Mie scattering are especially important for a few nanometer to submicron-sized objects.

2.1 Optical properties of particles

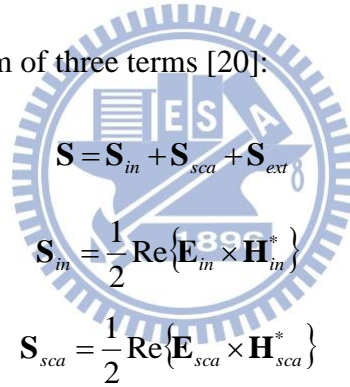
2.1-1 Mie theory

Light scattering by an induced dipole moment is caused by an incident electromagnetic wave. Electromagnetic field of an arbitrary particle (E , H) located at the polar coordination system can be expressed by the combination of incident electromagnetic field (E_{in} , H_{in}) and

scattering electromagnetic field (\mathbf{E}_{sca} , \mathbf{H}_{sca}).

$$\mathbf{E} = \mathbf{E}_{in} + \mathbf{E}_{sca} \quad \mathbf{H} = \mathbf{H}_{in} + \mathbf{H}_{sca} \quad (\text{Eq. 2-1})$$

The Poynting vector $\mathbf{S} = \mathbf{E} \times \mathbf{H}$ specifies the magnitude and direction of the rate of the transfer of electromagnetic energy at all points of spaces. Once we have obtained the electromagnetic fields inside the particle and scattered by the particle, we can determine the Poynting vector at any point. However, we are usually interested only in the points outside the particle. The time-averaged Poynting vector \mathbf{S} at any point in the medium surrounding the particle can be written as the sum of three terms [20]:



$$\mathbf{S} = \mathbf{S}_{in} + \mathbf{S}_{sca} + \mathbf{S}_{ext}$$

$$\mathbf{S}_{in} = \frac{1}{2} \text{Re} \{ \mathbf{E}_{in} \times \mathbf{H}_{in}^* \}$$

$$\mathbf{S}_{sca} = \frac{1}{2} \text{Re} \{ \mathbf{E}_{sca} \times \mathbf{H}_{sca}^* \}$$

$$(\text{Eq. 2-2})$$

$$\mathbf{S}_{ext} = \frac{1}{2} \text{Re} \{ \mathbf{E}_{in} \times \mathbf{H}_{sca}^* + \mathbf{E}_{sca} \times \mathbf{H}_{in}^* \} \quad (\text{Eq. 2-3})$$

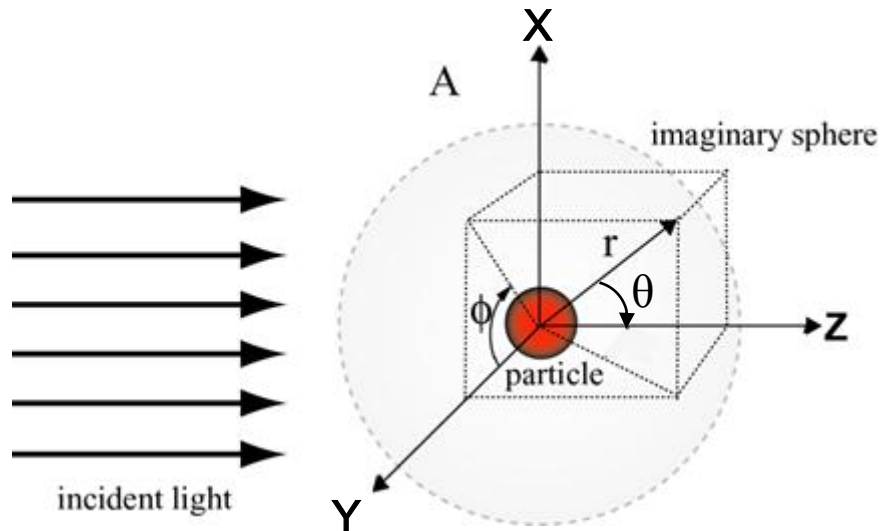


Figure 2.1 Spherical polar coordinate system centered on a spherical particle of radius a .

If the orientation of a plane surface with area A is specified by a unit normal vector N , the net rate W at which electromagnetic energy crosses the boundary of a closed surface A which enclose a volume V is

$$W_a = -\int_A \mathbf{S} \cdot \mathbf{e}_r dA \quad (\text{Eq. 2-4})$$

If $W_a > 0$ (if W_a is negative, energy is being created within the sphere), energy is absorbed within the sphere. But the medium is non-absorbing, which implies that W_a is the rate at which energy is absorbed by the particle. Because of Eq. 2-4, W_a may be written as the sum of three terms [20]:

$$W_{abs} = W_{in} - W_{sca} + W_{ext} \quad (\text{Eq. 2-5})$$

where

$$W_{in} = -\int_A \mathbf{S}_{in} \cdot \mathbf{e}_r dA, \quad W_{sca} = \int_A \mathbf{S}_{sca} \cdot \mathbf{e}_r dA, \quad W_{ext} = -\int_A \mathbf{S}_{ext} \cdot \mathbf{e}_r dA \quad (\text{Eq. 2-6})$$

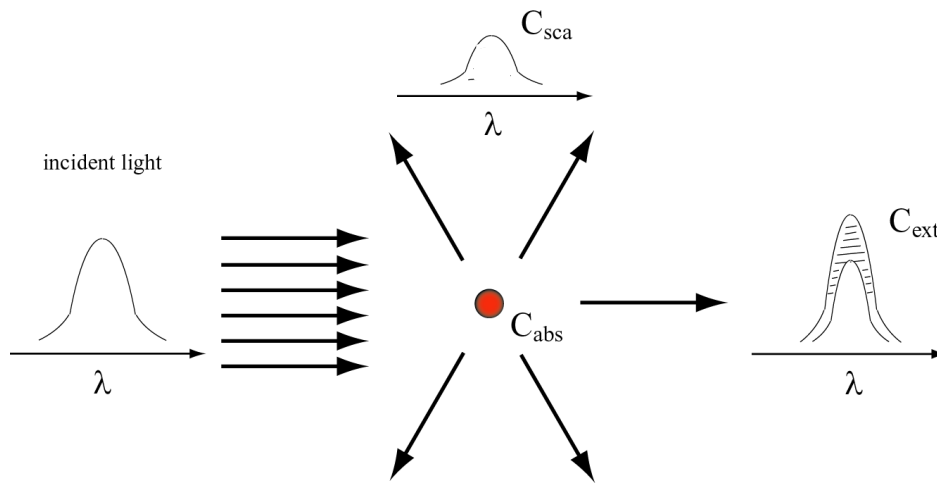


Figure 2.2 Light scattering, absorption, and extinction by a single particle, whose cross sections are given as C_{sca} , C_{abs} , and C_{ext} respectively.

W_{in} vanishes identically for a non-absorbing medium; W_{sca} is the rate at which energy scattered across the surface A . Therefore, W_{ext} is just the sum of the energy absorption rate and the energy scattering rate which corresponds extinction by particle:

$$W_{ext} = W_{sca} + W_{abs} \quad (\text{Eq. 2-7})$$

The ratio of W_{ext} to I_i is a quantity with dimensions of area called cross section:

$$C_{ext} = \frac{W_{ext}}{I_i} \quad (\text{Eq. 2-8})$$

where I_i is the incident irradiation.

Similarly to Eq. 2-7, the extinction cross section C_{ext} can be written as the sum of the absorption cross section C_{abs} and the scattering cross section C_{sca} :

$$C_{ext} = C_{abs} + C_{sca} \quad (\text{Eq. 2-9})$$

Based on physics, we know that W_{ext} and W_a are independent of the polarization state of the incident light. Therefore, we may take the incident light to be x-polarized [20]:

$$\begin{aligned} E_{i\theta} &= \frac{\cos \phi}{\rho} \sum_{n=1}^{\infty} E_n (\psi_n \pi_n - i \psi'_n \tau_n), \quad H_{i\theta} = \frac{k}{\omega \mu} \tan \phi E_{i\theta} \\ E_{i\phi} &= \frac{\sin \phi}{\rho} \sum_{n=1}^{\infty} E_n (i \psi'_n \pi_n - \psi_n \tau_n), \quad H_{i\phi} = \frac{-k}{\omega \mu} \cot \phi E_{i\phi} \end{aligned}$$

(n=1, 2, ...) (Eq. 2-9)

where ω is angular frequency, μ is permeability and $\rho = kr$. The angle dependent functions π_n , τ_n and ψ_n are

$$\pi_n(\theta) = \frac{P_n^1(\cos \theta)}{\sin \theta}, \quad \tau_n(\theta) = \frac{dP_n^1(\cos \theta)}{d\theta}, \quad \psi_n(\theta) = \rho J_n(\rho) \quad (\text{Eq. 2-10})$$

where $P_n^1(\cos \theta)$ is associated Legendre function and $J_n(\rho)$ is the first term of Bessel function.

The corresponding scattered field is

$$\begin{aligned} E_{s\theta} &= \frac{\cos \phi}{\rho} \sum_{n=1}^{\infty} E_n (ia_n \xi'_n \tau_n - b_n \xi_n \pi_n), \quad H_{s\theta} = \frac{k}{\omega \mu} \frac{\sin \phi}{\rho} \sum_{n=1}^{\infty} E_n (ib_n \xi'_n \tau_n - a_n \xi_n \pi_n) \\ E_{s\phi} &= \frac{\sin \phi}{\rho} \sum_{n=1}^{\infty} E_n (b_n \xi_n \tau_n - ia_n \xi'_n \pi_n), \quad H_{s\phi} = \frac{k}{\omega \mu} \frac{\cos \phi}{\rho} \sum_{n=1}^{\infty} E_n (ib_n \xi'_n \pi_n - a_n \xi_n \tau_n) \end{aligned}$$

$\xi_n = \rho h_n(\rho)$ (n=1, 2, ...) (Eq. 2-11)

And the scattering coefficients of the field inside the particle are [20]

$$a_n = \frac{\mu m^2 j_n(mx) [x j_n(x)] - \mu_p m^2 j_n(x) [mx j_n(mx)]}{\mu m^2 j_n(mx) [x h_n^{(1)}(x)] - \mu_p h_n^{(1)}(x) [mx j_n(mx)]}$$

$$b_n = \frac{\mu_p m^2 j_n(mx) [x j_n(x)] - \mu j_n(x) [mx j_n(mx)]}{\mu_p j_n(mx) [x h_n^{(1)}(x)] - \mu h_n^{(1)}(x) [mx j_n(mx)]} \quad (\text{Eq. 2-13})$$

where $h_n^{(l)}(\rho)$ is Hankel function, $j_n(x)$ is spherical Bessel function and μ_l, μ are permittivities of the particle and medium.

The size parameter and the refractive index are expressed as

$$x = \frac{2\pi N_{env} a}{\lambda}, \quad m = \frac{N_l(\lambda)}{N_{env}} \quad (\text{Eq. 2-14})$$

where N_l and N are refractive indices of particle and medium, respectively; a is the radius of particle, λ is the wavelength of incident light.

Together with Eq. 2-6, Eq. 2-10 and Eq. 2-12, we derive expressions for the cross sections of a sphere more exactly:

$$W_{ext} = \frac{1}{2} \text{Re} \int_0^{2\pi} \int_0^\pi (\mathbf{E}_{i\phi} \mathbf{H}_{s\theta} - \mathbf{E}_{i\theta} \mathbf{H}_{s\phi} - \mathbf{E}_{s\theta} \mathbf{H}_{i\phi} + \mathbf{E}_{s\phi} \mathbf{H}_{i\theta}) r^2 \sin \theta d\theta d\phi$$

$$W_{sca} = \frac{1}{2} \text{Re} \int_0^{2\pi} \int_0^\pi (\mathbf{E}_{s\theta} \mathbf{H}_{s\phi} + \mathbf{E}_{s\phi} \mathbf{H}_{s\theta}) r^2 \sin \theta d\theta d\phi \quad (\text{Eq. 2-15})$$

Then the scattering cross section is obtained [20]:

$$C_{sca} = \frac{2\pi}{k^2} \sum_{n=1}^{\infty} (2n+1) (|a_n|^2 + |b_n|^2) \quad (\text{Eq. 2-16})$$

Similarly, the extinction cross section is:

$$C_{ext} = \frac{2\pi}{k^2} \sum_{n=1}^{\infty} (2n+1) \text{Re}\{a_n + b_n\} \quad (\text{Eq. 2-17})$$

2.1-2 Rayleigh scattering

Expanding the spherical Bessel functions in the scattering coefficients leads a_n and b_n to power series. Retaining the scattering coefficients in a sufficient number of expansions, the four coefficients can be obtained as [20]

$$a_1 = -\frac{i2x^3}{3} \frac{m^2 - 1}{2m^2 + 2} - \frac{i2x^5}{5} \frac{(m^2 - 2)(m^2 - 1)}{(m^2 + 2)^2} + \frac{4x^6}{9} \left(\frac{m^2 - 1}{m^2 + 2}\right)^2 + O(x)$$

$$b_1 = -\frac{ix^5}{45} (m^2 - 1) + O(x^7), \quad a_2 = -\frac{ix^5}{15} \frac{m^2 - 1}{2m^2 + 3} + O(x^7), \quad b_2 = O(x^7) \quad (\text{Eq. 2-16})$$

Here, we have taken permittivity of the sphere to be equal to that of the surrounding medium.

If $|m| x \ll 1$, then $|b_l| \ll |a_l|$; with this assumption the amplitude scattering matrix elements are down to terms of order x^3 .

If the incident light is unpolarized with irradiance I_i , the scattered irradiance I_s calculated by scattering matrix is

$$I_s = \frac{8\pi^4 N a^6}{\lambda^4 r^2} \left| \frac{m^2 - 1}{m^2 + 2} \right| (1 + \cos^2 \theta) I_i \quad (\text{Eq. 2-17})$$

Thus, if the quantity $|(m^2-1)/(m^2+2)|$ is weakly dependent on wavelength, the irradiance scattered by a sphere small compared with the wavelength or, indeed, any sufficiently small particle regardless of its shape, is proportional to $1/\lambda^4$.

“When light is scattered by particles which are very small compared with any of the wavelengths, the ratio of the amplitudes of the vibrations of the scattered and incident light varies inversely as the square of the wavelength and the intensity of the lights themselves as the inverse fourth power.” Lord Rayleigh showed the simple dimensional analysis in 1871.

However, if the incident light is unpolarized, the scattered light will be partially polarized. Thus, we defined the degree of polarization of the scattered light, $|P|$, which is independent of particle size.

$$P = \frac{1 - \cos^2 \theta}{1 + \cos^2 \theta} \quad (\text{Eq. 2-18})$$

The extinction and scattering cross sections are

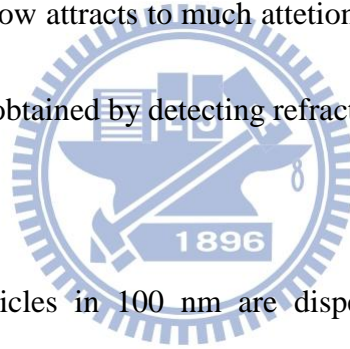
$$C_{ext} = k \operatorname{Im}\{\alpha\} = \pi a^2 4x \operatorname{Im}\left\{\frac{m^2 - 1}{m^2 + 2}\right\}$$

$$(Eq. 2-19) \quad C_{sca} = \frac{k^4}{6\pi} = \pi a^2 \frac{8}{3} x^4 \left|\frac{m^2 - 1}{m^2 + 2}\right|^2$$

(Eq. 2-20)

2.1-3 Refractive index of metallic and organic nanoparticles

The optical property of metallic nanoparticle is strongly dependent on particle size, shape, electron density and the local environment, the refractive index of surrounding medium. The application of refractive index now attracts much attention because other parameters such as density and temperature can be obtained by detecting refractive index [21].



We consider Au nanoparticles in 100 nm are dispersed on the glass substrate and embedded in non-absorbing medium. The relationship between the shift of surface plasmon band and the refractive index was given by

$$\Delta\lambda_{\max} = m\Delta n \left[1 - \exp\left(\frac{-2d}{l_d}\right) \right] \quad (Eq. 2-20)$$

Here m is the bulk refractive-index response of the nanoparticle(s); Δn is the change in refractive index induced by the adsorbate; d is the effective adsorbate layer thickness; and l_d is the characteristic EM-field-decay length (approximated as an exponential decay) [22].

Herman suggested the scattering efficiency based on Mie theory could be written [23]:

$$\lim_{x \rightarrow \infty} Q_{sca} = 1 + R(0^\circ) \quad (\text{Eq. 2-21})$$

where $R(0^\circ) = |(m-1)/(m+1)|^2$ is a reflectance of a plane surface at normal incidence and m is the complex relative refractive index of nanoparticle [24].

Fig. 2.3 shows the calculated scattering spectra of gold nanoparticle with various refractive index of surrounding medium from 1.33 to 1.53. Based on Mie theory, the calculation result displays that the surface plasmon band red-shifts and the scattering efficiency enhances as the refractive index increases.

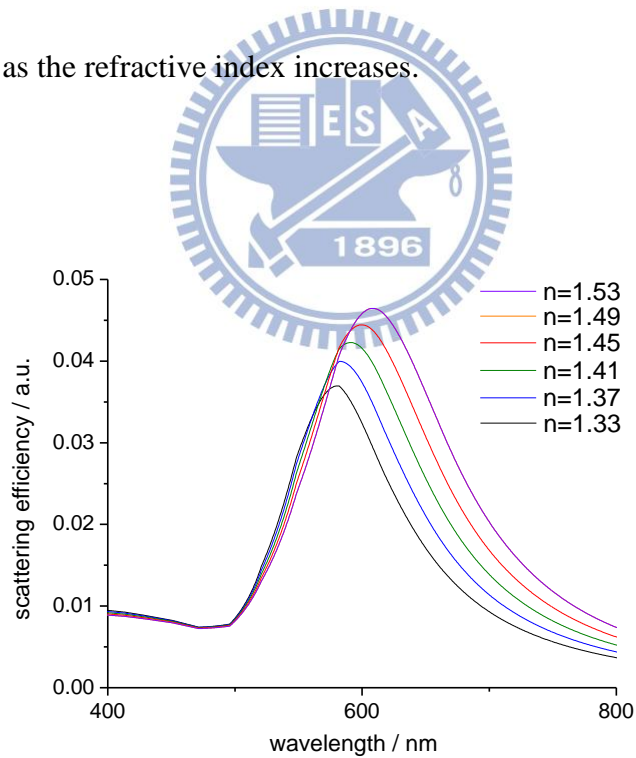


Figure 2.3 Calculated spectra of 100 nm Au nanoparticles with various refractive index. With the increase of refractive index, the plasmon band shifts to longer wavelength, the intensity increases, and the FWHM of the plasmon band broadens.

Chapter 3 Experimental setup

3.1 Light source

Mode-locked Ti: sapphire laser light (wavelength; 700-900 nm, repetition rate; 80 MHz, pulse duration; 160 fs, Tsunami, Spectra Physics) was introduced into a photonic crystal fiber (PCF) to generate supercontinuum femtosecond laser beam, which was used as the light source in this study. In principle, the Ti: sapphire laser (Fig. 3.1) was pumped by a continuous wave solid-state visible laser (wavelength; 532 nm, Millennia Pro, Spectra Physics) at around 7 W and was controlled by an electronics module (Model 3955, Spectra Physics). A prism sequence and a slit were used for dispersion control and wavelength selection (Fig. 3.2), respectively. Spectral information of the output laser light was provided by a fiber optic spectrometer (USB4000, Ocean Optics). Full width at half maximum of the spectrum and central wavelength of the laser light were adjusted to be about 12 nm and 800 nm simultaneously, and then the laser light was focused on PCF (Fig. 3.3).

PCF (core diameter; 1.8 μm , zero dispersion wavelength; 750 nm; length; 100 cm, NL-PM-750, Crystal Fibre) use a microstructured cladding region with air holes to guide light in a pure silica core, which allows laser through a cascade of nonlinear effects to give rise to a spectrum extending from the visible to the near infrared (Fig. 3.4).

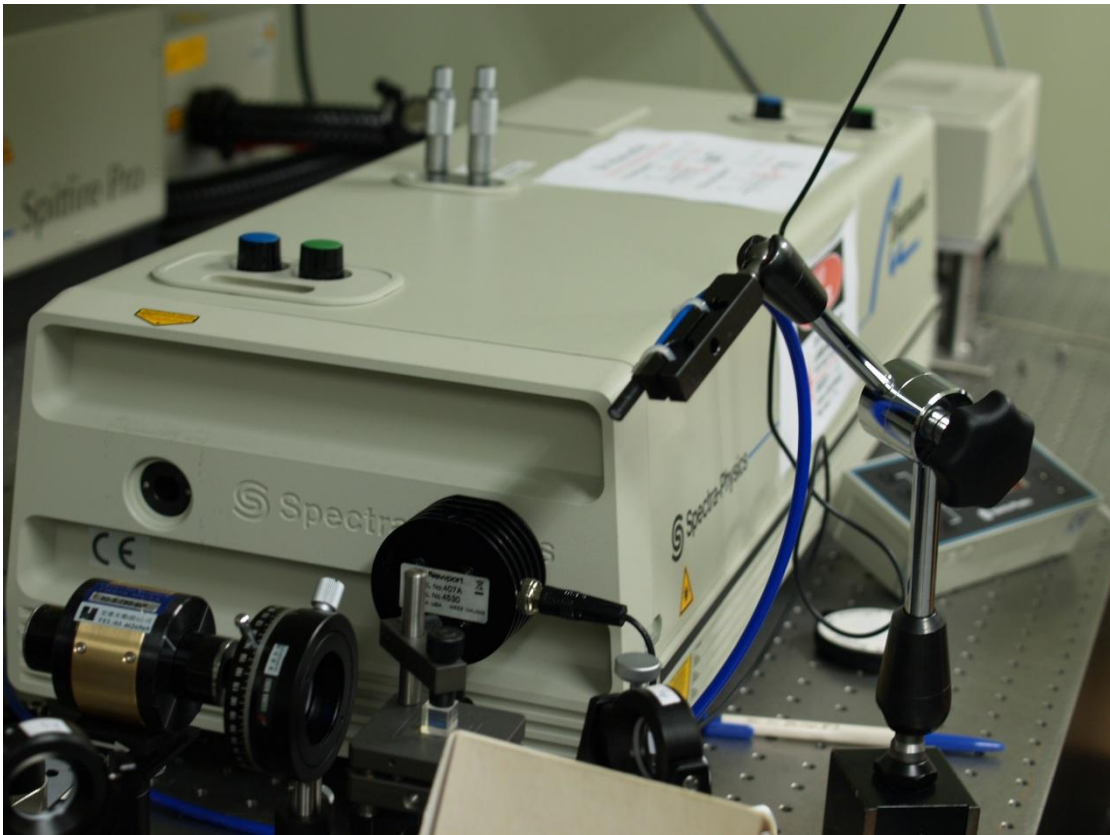


Figure 3.1 A picture of mode-locked Ti:sapphire laser, Tsunami

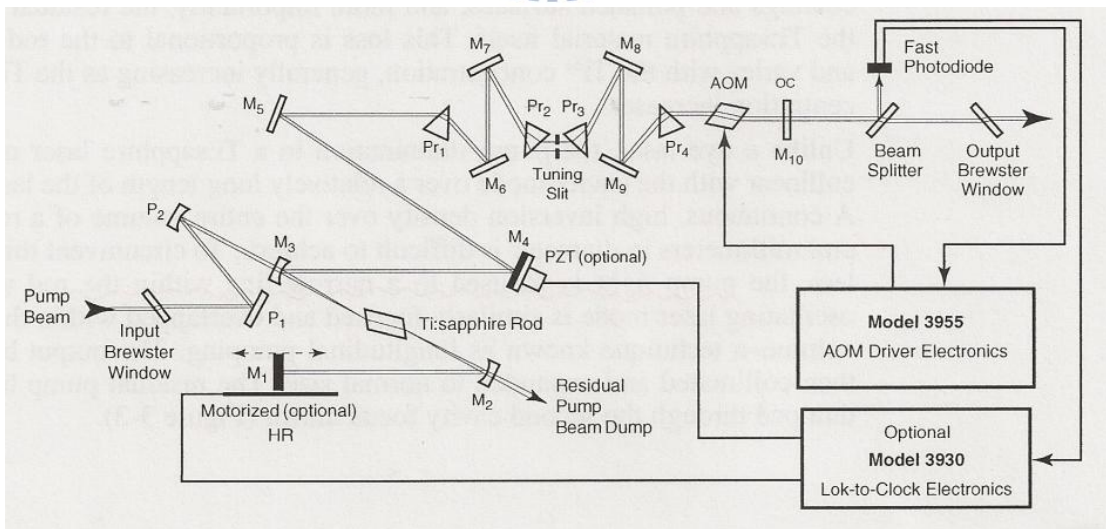


Figure 3.2 The setup for mode-locking

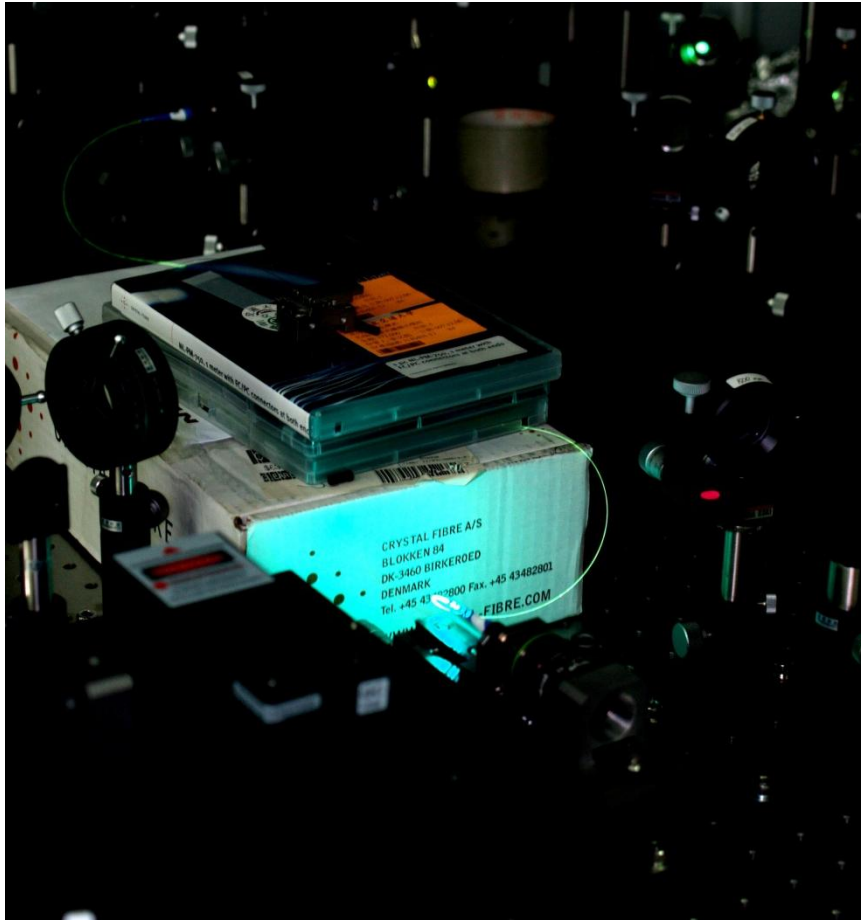


Figure 3.3 A picture of shining photonic crystal fiber due to supercontinuum

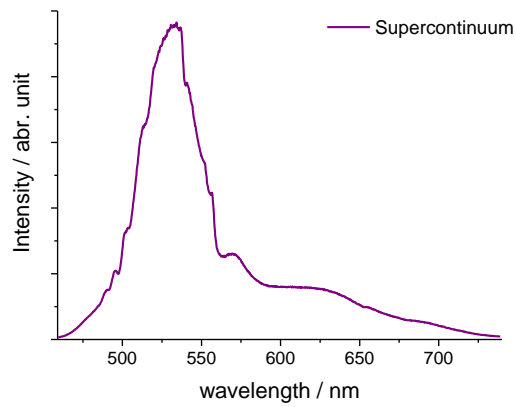


Figure 3.4 One example of the light intensity profile of generated supercontinuum

3.2 Confocal Rayleigh scattering microspectroscopic imaging system

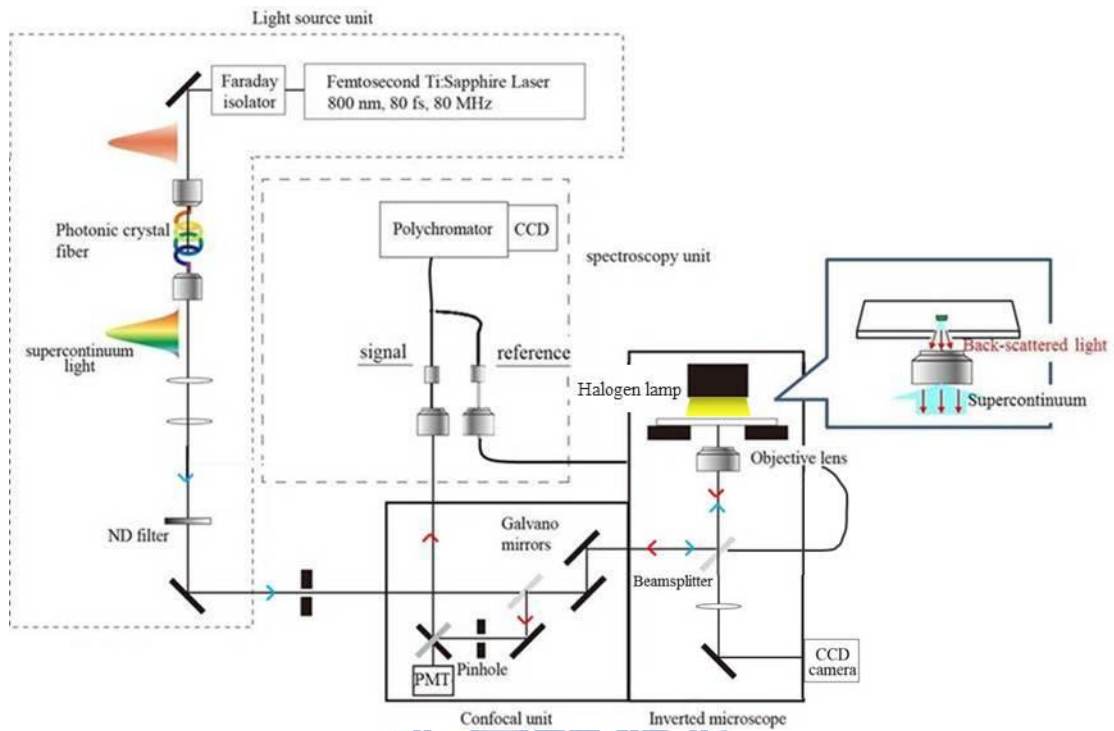


Figure 3.5 The schematic illustration of our confocal Rayleigh scattering microspectroscopic and imaging system. Blue and red arrows represent illumination and back scattering.

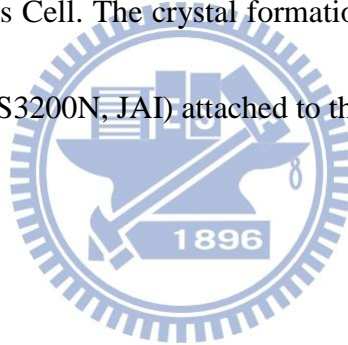
Fig. 3.5 showed a schematic illustration of our confocal Rayleigh scattering microspectroscopic and imaging system. The system is based on the confocal microscope set up containing an inverted microscope (IX71, Olympus) and scanning units (FV300, Olympus). The supercontinuum light output from the PCF was divided into two beams by a beam splitter, one was introduced into a polychromator (SpectraPro 2300i, Princeton Instruments) coupled with a charge-coupled device (PIXIS 400, Princeton Instruments) as reference light and the other was focused on the sample, using an oil immersion objective lens (100 \times , N.A. 1.35,

Olympus) as a probe light. The Olympus objective lenses and optics have been designed to suppress the chromatic chirp and aberration. Besides we used an immersion oil (with refractive index = 1.5) to suppress further aberration effect between the objective lens and sample chamber. Thus, we consider that our data are almost free of chromatic aberration.

The scattered light from sample was collected by the same objective lens and then passed through a pinhole which was used to measure the target single grana selectively by the polychromator-CCD system. The setup allows us to measure Rayleigh back scattering which only from the single granum at the focal plane can pass through the pinhole. This means we can exclude the contribution of light absorption greatly to the scattering measurements. Secondly, we discuss anisotropic structures and its size-dependences based on the Soret-band, but the fluorescence comes from the Q-band and so large Stokes shift means that Rayleigh light scattering corresponding to the Soret-band is not affected by the fluorescence. To convert the scattering light into scattering efficiency, we first subtracted the noise signal from scattering signal then divided the difference by the reference light.

3.3 Experimental setup for crystallization

Linearly polarized femtosecond laser pulses from femtosecond laser (wavelength; 800 nm, pulse duration; 160 fs, Spitfire Pro, Spectra Physics) were introduced to an inverted microscope (IX-71, Olympus) through an objective lens (10×, N. A. 0.25, PlanN, Olympus). Pulse energy was adjusted by using a half-wave plate, a polarizing beam splitter, and a variable neutral density filter, and then was measured after passing through an objective lens by energy meter (842-PE, Spectra Physics). The repetition rate of femtosecond laser pulse train was controlled by a Pockels Cell. The crystal formation and morphology were observed with a digital CCD camera (CV-S3200N, JAI) attached to the microscope [25].



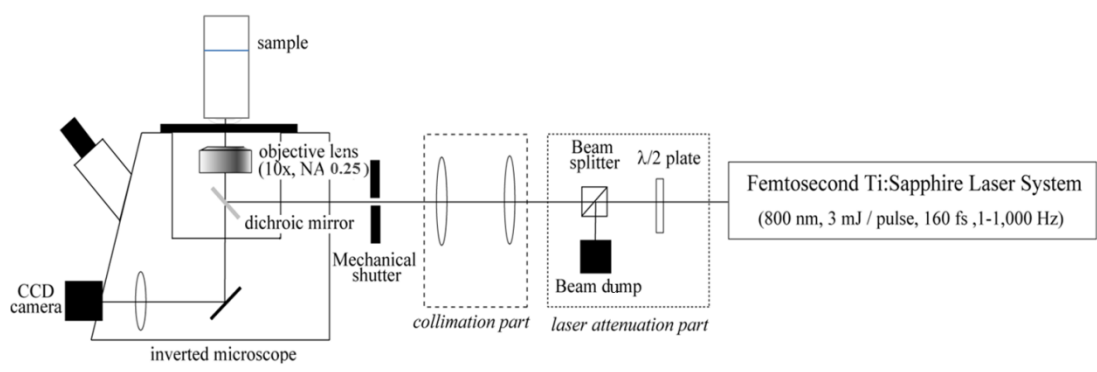


Figure 3.6 Laser light source and microscopic system for crystallization.



Figure 3.7 A picture of inverted microscope and other accessories.

Chapter 4 Three dimensional morphological and spectroscopic study of *Egeria densa*

The light scattering microscopy of metallic or organic NPs has been well investigated for decades. Theoretical and experimental studies have provided established fundamental concepts of light scattering dynamics, microscopy, and imaging of NPs. One of interesting features of this technique is that the scattering spectrum can give us information on the shape, size, refractive index, electron density of the target particles, as well as the refractive index of the medium. Thus, by utilizing such a technique with grana of plant cells being the target particles, we study optically and spectroscopically the configuration and size of *in vivo* grana.



For this purpose, we have used *Egeria densa* Planchon (*Hydrocharitaceae*), commonly known as Brazilian elodea or common waterweed, as the target. This submersed perennial plant species native to south-eastern America was selected due to its well-known “ecosystem engineer,” given its role in stabilizing sediment and reducing turbidity and its important role in trophic dynamics [26]. The alga with a 2 cell thick leaf was cultivated in an aquarium in our lab (Fig. 4.1). To maintain the healthiness of the alga, visually indicated by its growth and green leaves, we set the aquarium in light area and exchange the water medium once a week.



Figure 4.1 A picture of *Egeria densa* in the aquarium.

4.1 Sample preparation

The sample was prepared by sandwiching a section of 1 mm × 3 mm of green leaf of *E. densa* with two cover slips (18 mm × 18 mm and 24 mm × 40 mm, Mastsumami). The gap of the cover slips was filled with water to keep it wet, and it was sealed with a nail polish to avoid evaporation. The typical sample cell containing the green cell of *E. densa* is shown in

Fig. 4.2.

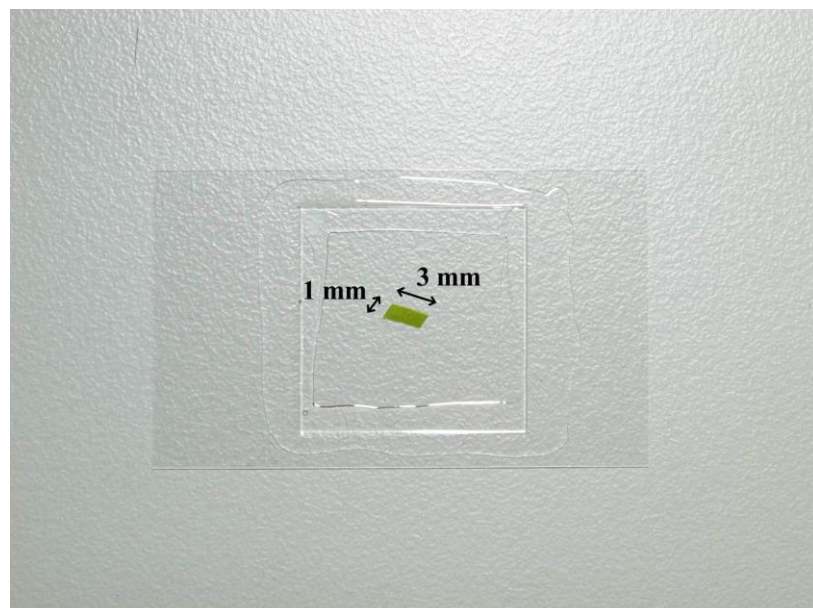


Figure 4.2 A sample in dimension of 1 mm × 3 mm was cut by scissor. The upper and top glass substrates were 24 mm × 40 mm and 18 mm × 18 mm, respectively. Additional water and nail polish to seal glasses were used to keep plant alive.

Under bright and dark field (with objective lens 100×, N.A. =1.4), the plant cells in the leaf are observed as “islands” with white and dark-green area respectively (Fig. 4.3). More specifically, by dark-field imaging, chloroplasts are easily distinguished and each cell is bordered by cell wall which can be seen obviously. Dark-field image also shows higher contrast that could be a great help of observation.

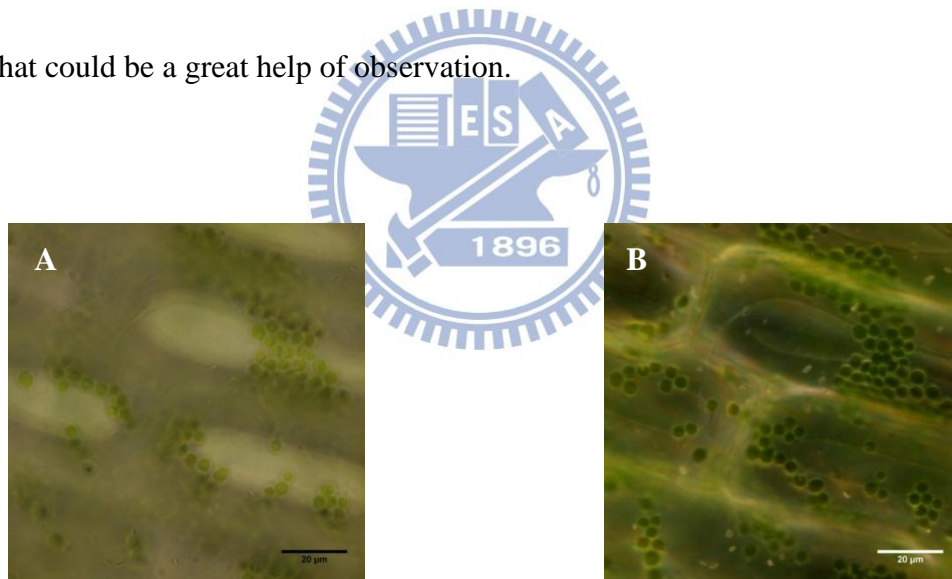
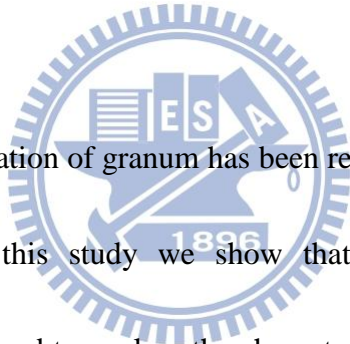


Figure 4.3 (A) Bright field and (B) dark field images of plant cell of *Egeria densa*

4.2 Results and discussion

4.2-1 Three dimensional morphological analysis of *Egeria densa*

By changing detection system to confocal microscopy, with the objective lens 100 \times , N.A.= 1.4, we are able to observe a single granum in more detail. Granum, single grana, is composed of stacked discoidal membranous system called thylakoids where all the molecular complexes that drive the light-induced reaction and provide a medium for energy transduction are located.

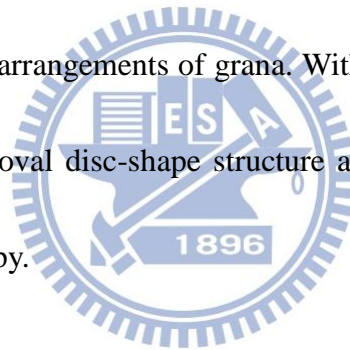


Though such a 3-D organization of granum has been revealed by high resolution electron tomography [16, 18, 32], in this study we show that our optical, spectroscopic and non-destructive method can be used to explore the characteristic of grana. The architecture of grana provides insights into their formation and function to clarify light-harvesting and electron transport.

Thylakoid membranes could not be recognized by our system. However, distinguishing each single granum *in vivo* is quite easy. Confocal light scattering spectroscopic images of a living plant cell with different magnifications are shown in Figs. 4.4 ~ 4.6. Fig. 4.4 shows the structure of the cells; the rectangles represent the cell walls, and many bright spots forming a

circle is regarded as a chloroplast, hence those gathering spots are grana while other isolated bright spots are organelles. In some cells, only few chloroplasts were found, which suggests the organelles moved freely due to living cell. Also, it depicts the construction of chloroplasts and the different brightness of spots shows the spatial distribution of grana.

By scanning microscope objective along the z-axis from the bottom to the top within a cell, we obtained two dimensional image stack with different height and constructed three dimensional images of chloroplasts (Fig. 4.7). Three dimensional images not only reflect the depth of a cell but illustrate the arrangements of grana. With confocal light scattering images, we found that chloroplasts are oval disc-shape structure and diverse size, which have been confirmed by electron microscopy.



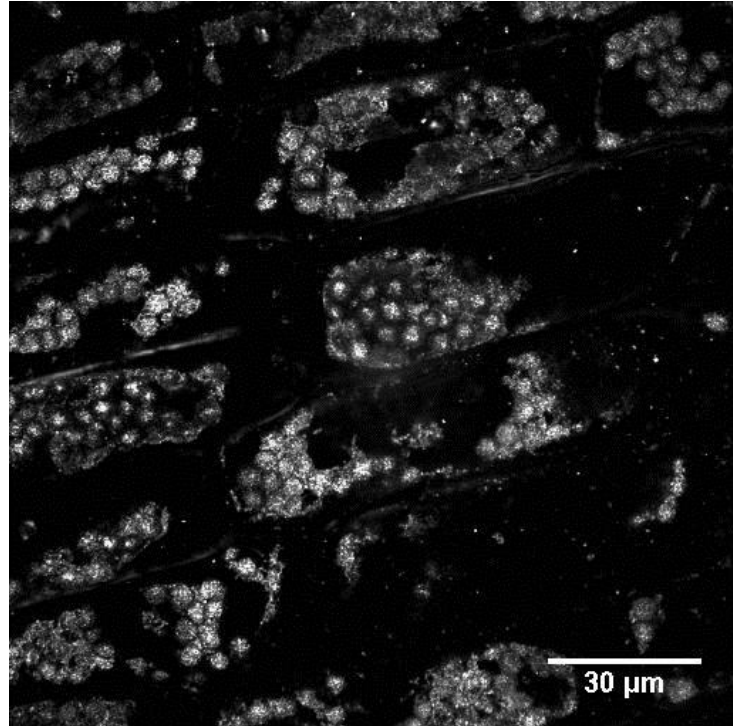


Figure 4.4 Light scattering image of plant cell of *Egeria densa* without zooming in.

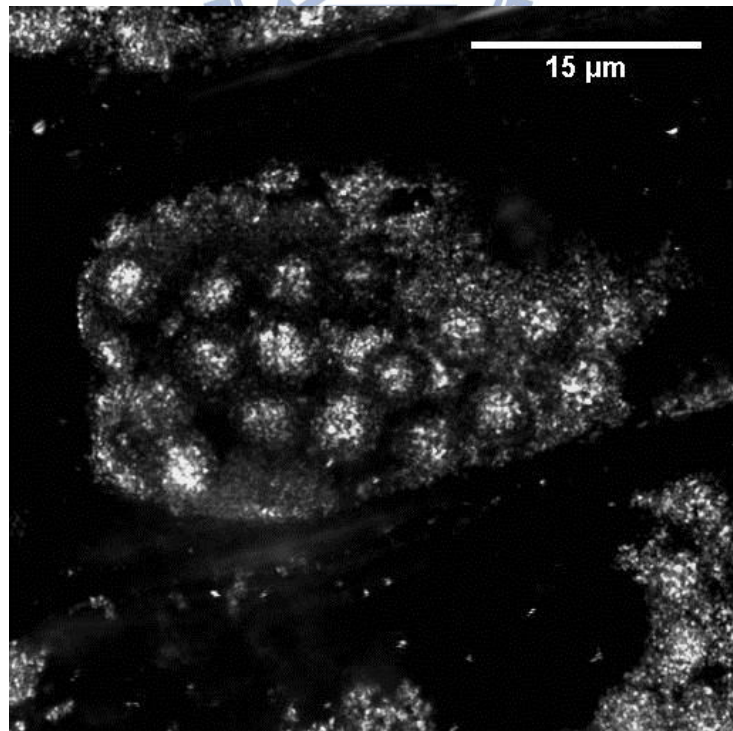


Figure 4.5 Light scattering image of plant cell of *Egeria densa* with three times zoom.

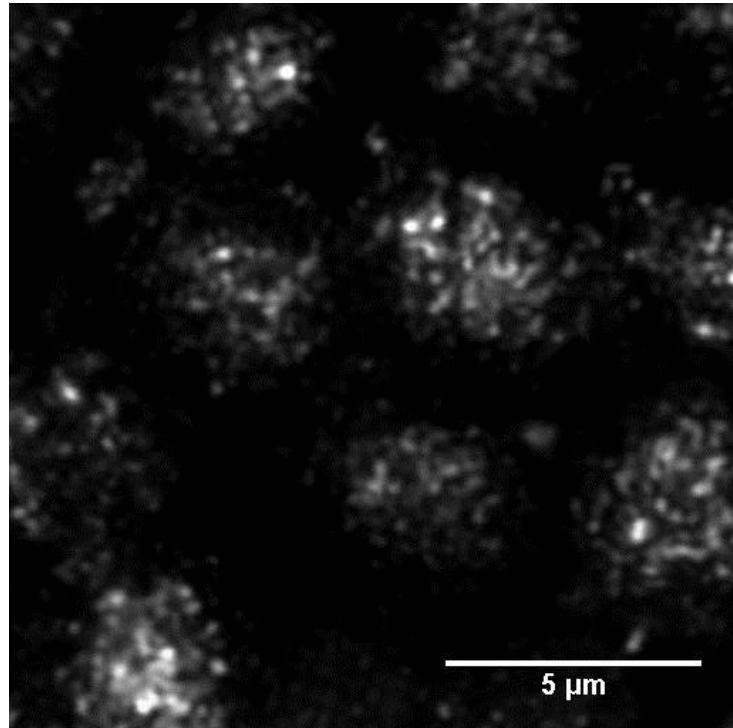


Figure 4.6 Light scattering image of plant cell of *Egeria densa* with ten times zoom.

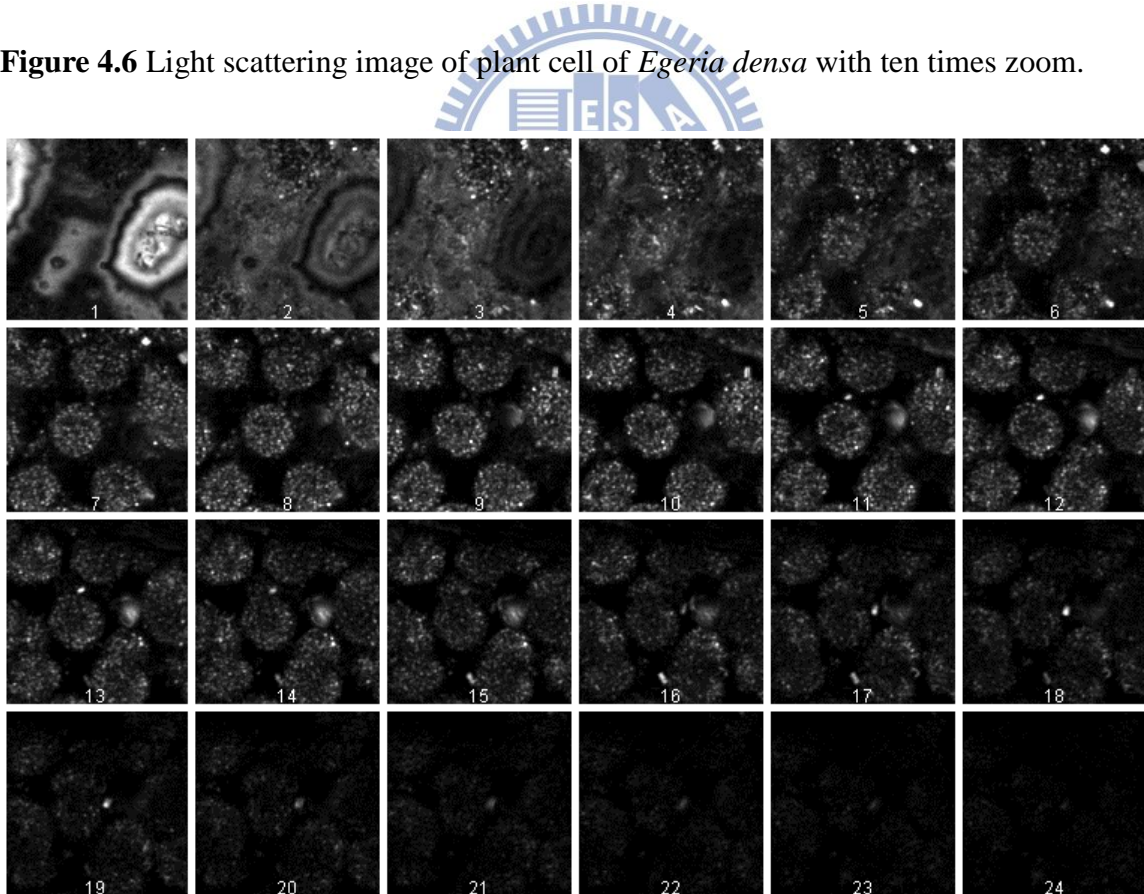


Figure 4.7 Confocal light scattering spectroscopic images of *Egeria densa* at different vertical positions, from the bottom to the top of the leaf with 0.2 μm per step.

The average size of the grana is examined by the line profile method on the basis of the obtained 3-D light scattering images. This practical way is useful for examining the relative behavior of all variables in a multivariate data set. The line profile plot consists of a sequence of equi-spaced vertical spikes with each spike representing a different variable in the multivariate data set. In this case, each spike is corresponding to the pixel intensity of the granum in the X-Y image as shown in Fig. 4.8 (A). By fitting the light intensity profile of granum with the Gaussian fit, we can obtain the size which is derived from the FWHM, full width at half maximum, of the Gaussian curve. The grana we estimated were on the focal plane. In conclusion, the average size of the grana was approximated as 273 nm for 1000 numbers of grana. In order to determine the sensitivity and lateral resolution, we used small Au NPs. The cross section of a 40 nm Au NP allowed us to determine the lateral point spread function (PSF) with FWHM of the PSF of light, Δ [27]. Δ is calculated by $\Delta = \sqrt{\Delta_1^2 - \Delta_2^2}$, where Δ_1 is the FWHM of Gaussian function which was used to fit the intensity profile from confocal image of a 40 nm diameter Au NP, and Δ_2 is that of a model Gaussian function of the particle. In this experiment, Δ_1 and Δ_2 were 256 nm and 20 nm respectively, so Δ can be estimated to be 255 nm, which is better than $\lambda/2$ for the excitation wavelength, about 300 nm.

By the size analysis, not only the size distribution (Fig. 4.10) but also the spatial population could be resolved. We also found that on average, there are 100 grana distributed

randomly in the chloroplast of *E. densa*. From statistical analyses, both grana of the small size and the large one (Fig. 4.9) can be found in the center or on the surface of the chloroplast. The distribution of grana randomly in the chloroplast by this optical method is consistent with the direct observation by TEM imaging.

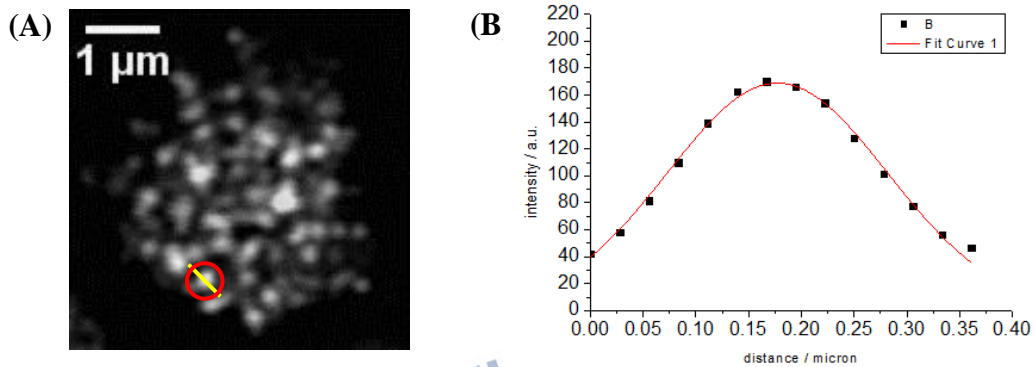


Figure 4.8 (A) A chloroplast image where a granum examined by us is marked as the red circle. (B) A measured scattering intensity profile (•) of (A) and its fitting curve by a Gaussian function (—). The FWHM calculated from Gaussian is used as the estimated size of granum. Since the distance between the close vicinity grana is small, we could not fit it with wider range, and could not have a clear zero background.

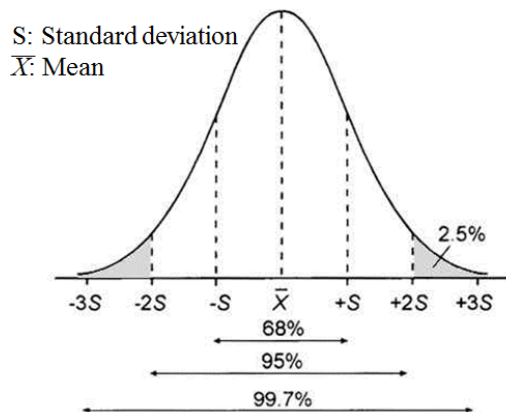


Figure 4.9 The definitions of small and large size. Grana below $-2S$ are small size and beyond $+2S$ are large size.

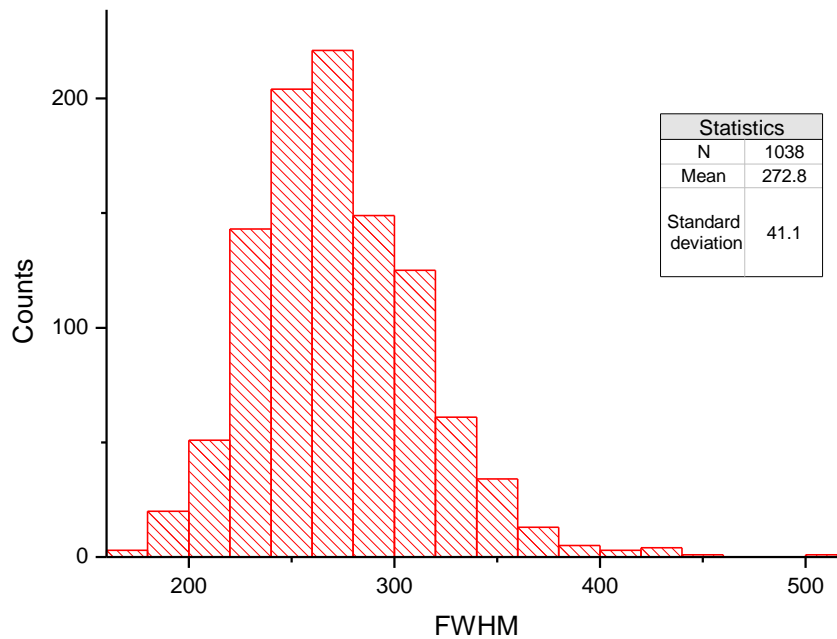
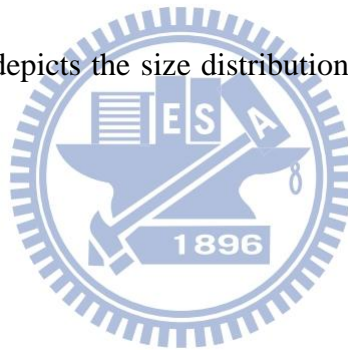


Figure 4.10 The statistic chart depicts the size distribution estimated for around 1000 grana, giving 273 nm as average size.



4.2-2 Confocal light scattering microspectroscopic analysis of grana in *Egeria densa*

The light scattering spectra show obvious Soret band located from 490~530 nm and the weak signal Q band can be found around 680 nm. Both bands are related to the absorption spectrum of chloroplasts, which contains two main bands; the Soret band is around 450 nm and the Q band is approximately at 650 nm. The difference is due to the relationship between absorption and scattering spectra. Fig. 4.11 illustrates the typical scattering spectrum of a single granum. The different size results in some side bands and relative intensity fluctuation,

indicating different assorted components inside the granum. By combination of light scattering images and scattering spectra to analyze the relationship between size and spectra, we found that the Soret band of the spectrum shifts to longer wavelength with the increasing size (Fig. 4.12 (B)). The range of the size starts from 200 nm to 460 nm and the Soret band of spectra shifts from 490 nm until 530 nm. Fig. 4.13 shows three types of the Soret band. When the band splits into two peaks, we considered both peaks and plotted the peak position of the Soret band against size (Fig. 4.14). It is clearly shown that the size and the Soret band wavelength presents a good correlation. The correlation implies that the red-shift is observed as the size is enlarged.

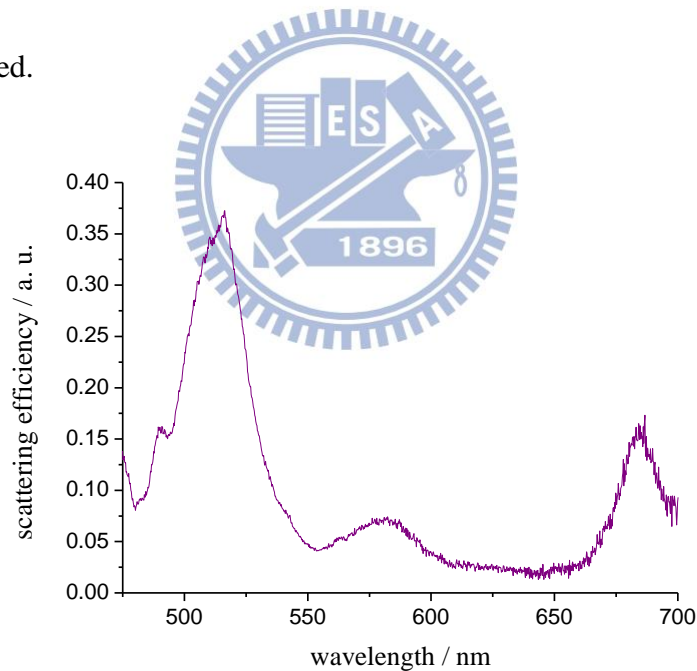


Figure 4.11 The light scattering spectrum of a granum.

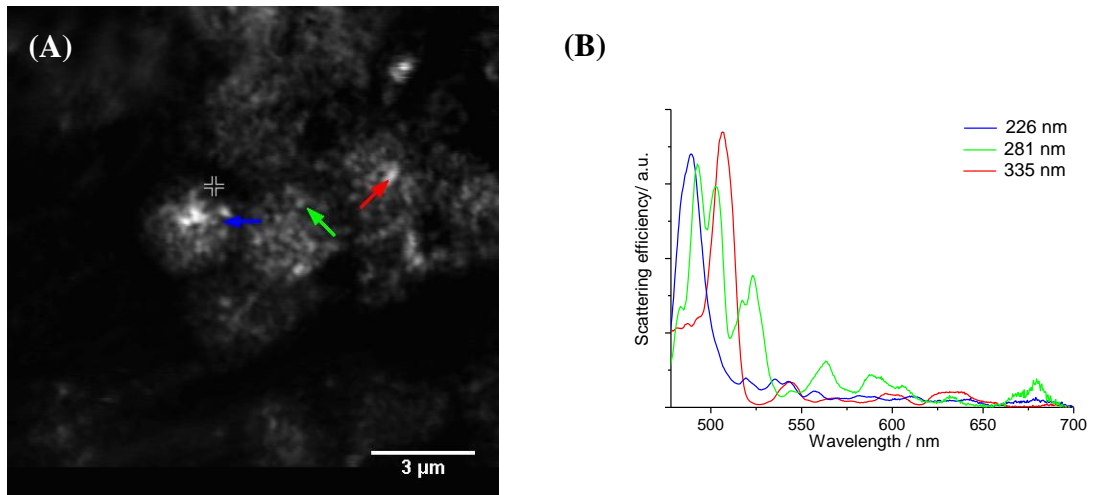


Figure 4.12 Light scattering image and spectra of single grana are shown. (A) Light scattering images of chloroplasts with 10 times magnification and (B) three spectra in different colors are related to single granum in (A), which differs from granum to granum.

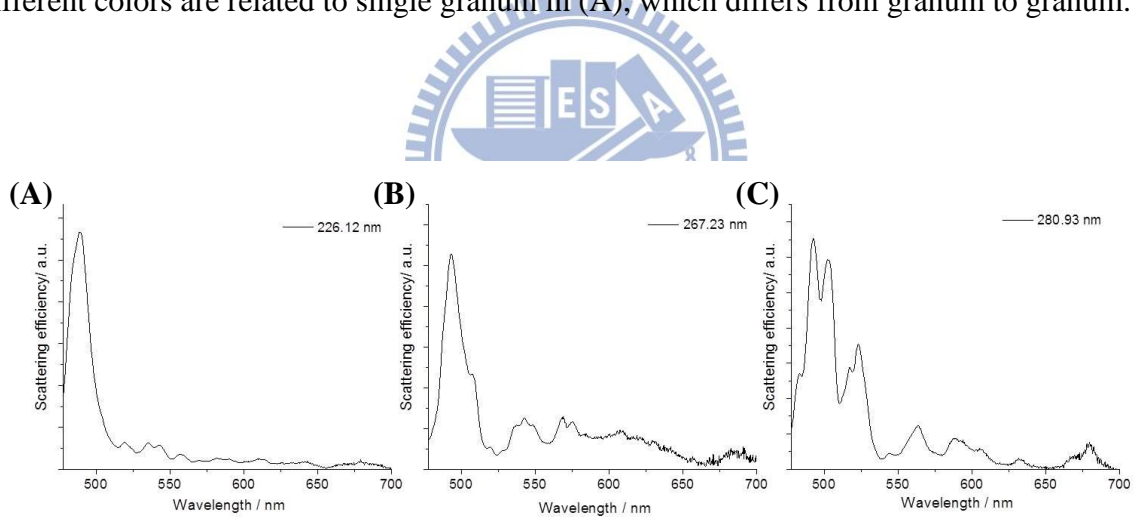


Figure 4.13 Light scattering spectra of grana. (A) The Soret band shows single peak. (B) The side peak of Soret band is small so we assumed this kind of peak as single peak. (C) The Soret band splits. We assumed the case as split peaks.

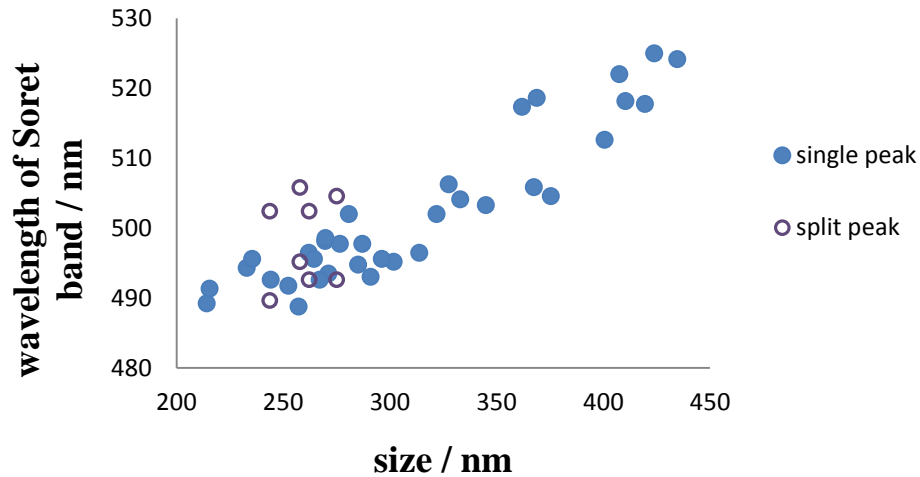
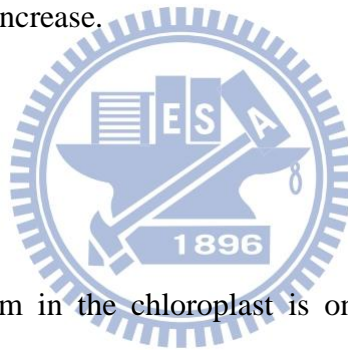


Figure 4.14 The plot of the peak wavelength of the Soret band against size. The split peaks correspond to the case C in Fig. 4.13. It is clearly shown that the Soret band shifts to longer wavelength as the size of grana increase.



Whether the site of granum in the chloroplast is one of the factors determining the scattering spectrum or not was confirmed by measuring the spectra of grana located at various site. First, we checked the position of chloroplast; we found that wherever chloroplast is either located, at the center, close to the cell wall, or in the alternative space in the leaf, the spectra of grana are not distinguishable. Moreover, the distribution of grana inside the chloroplast is not important. Fig. 4.15 (A) ~ (C) illustrate the position dependence of grana. It implies that the spectra of grana are independent on the position, although grana at the margin and at the center of chloroplast still show size dependence.

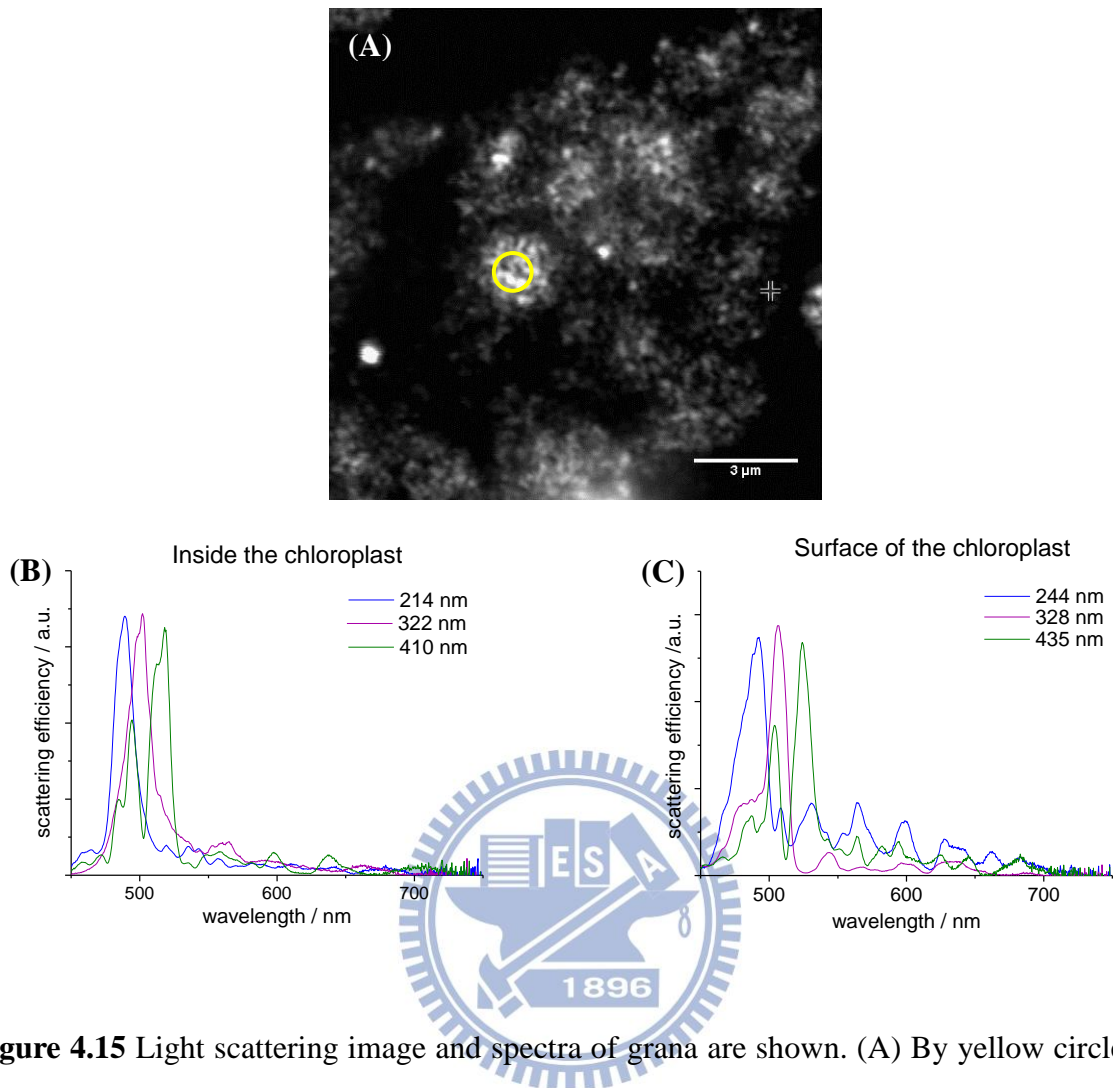


Figure 4.15 Light scattering image and spectra of grana are shown. (A) By yellow circle, we roughly defined the border of center and surface of the chloroplast. (B) The spectra of grana in the center of the chloroplast. (C) The spectra of grana at the surface of the chloroplast.

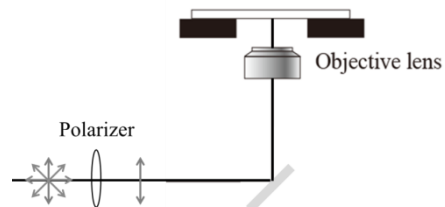


Figure 4.16 Polarizer is set in front of the confocal microscope. Each time we started from same angle as 0 degree; the polarization angle is relative.

The dependence of scattering spectrum of an individual granum on polarization of the probe light gives important information on the optical anisotropy of grana in the chloroplast. Such a method has been employed, for instance, in the study of optical anisotropy of chlorophyll molecules within *in vivo* chloroplasts [28]. Differential polarization imaging and circular dichroism provide information on long-range chiral organization of the pigment-protein complexes in mature granal chloroplasts [29]. In this study, the polarization measurement was operated by setting a polarizer in front of the microscope (Fig. 4.16). In other words, we expect that the polarized light interacts with molecules directly, and then the scattered light was transformed into signal in this measurement. Circular polarized supercontinuum passed through the polarizer and became a linear polarized input. The polarized angle is relative with respect to a certain angle in laboratory axis. To ensure the reliability of the polarization measurement of grana, at first we measured the scattering spectrum of 200 nm Au NP as a standard with essentially the same optical probe light and experimental setup.

The Au NPs are optically isotropic and exhibit high scattering efficiency in visible region due to the resonant plasma oscillation of conduction electrons. To minimize the contribution of the index-mismatched reflection, Au NPs are casted on the glass substrate and dipped in the immersion oil ($n = 1.5$) [30]. To analyze the polarization measurement data, we

plotted the scattering efficiency as a function of polarization angle (Fig. 4.17). The scattering efficiency was chosen from the fixed wavelength which was the Soret band of the unpolarized spectrum. Because Au NP is optical isotropic, polarization dependence of Au NP shows in Fig. 4.17 can be attributed to instrumental function. If we use depolarizer instead of instrumental function, we will not have any information on anisotropy of the grana or molecular alignment in the grana. By this instrumental function, we can therefore correct the raw data of polarization dependent measurement of grana.

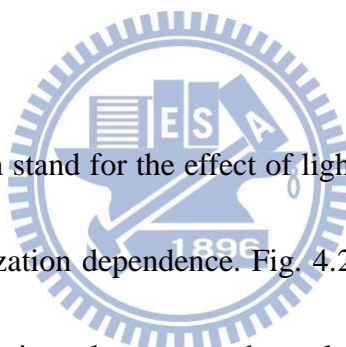
Fig 4.18 showed the spectra of single granum at polarization angles of 45, 90 and 135 degree. The spectra changed dramatically, especially at the Soret band. With the same analytical procedure with the case of Au NP, we found it hard to determine at which wavelength the scattering efficiency of granum should be analyzed, because the spectral shape also changed with polarization angle. As a consequence, we selected the wavelength from the unpolarized spectrum at which the scattering efficiency is maximum. After being corrected by instrumental function, we obtained the relative scattering intensity as a function of polarization angle, as shown in Fig. 4.19 (A). The polarization measurements of grana exhibit a band at 135 degree and a valley at 45 degree; that is to say that the Soret band appears and disappears depending on the angle of incident light with 90° symmetry, indicating optical anisotropy of grana. In Fig. 4.19 (B), we used polar coordinate system to depict the anisotropy

of grana efficiently. The solid and dotted lines represent experimental and expectation result, respectively, since the motion of living grana made measurement difficult.

Further analyses are expressed in Fig. 4.20 (A) and (B). For easier comparison, the maximum and minimum values of the polarization plot are defined as b and a , and the ratio of b and a (R), calculated as a/b , represents the change of light interacted by granum.

Fig. 4.20 (A) illustrates the parameter R as a function of the polarization angle at the peak wavelength of the Soret band, which shows clear correlation.

The FWHM which also can stand for the effect of light interacted by pigment molecules is used as a parameter of polarization dependence. Fig. 4.20 (B), which plots the FWHM of the primary band from polarization plot versus the polarization angle, trends down with correlation coefficient $r = -0.702$. The detail will be considered in discussion.



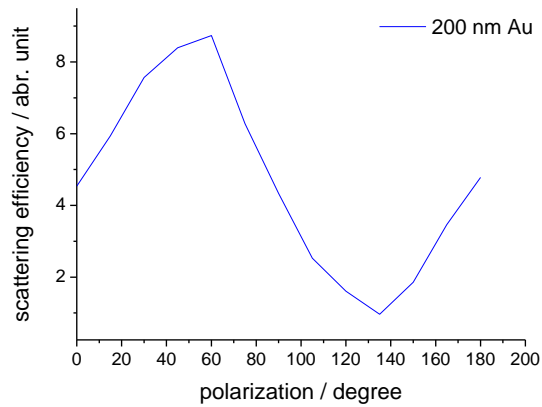


Figure 4.17 The polarization measurement of 200 nm Au NP. We measured the scattering efficiency of the resonance band at the wavelength giving its maximum intensity for each 15 degree. The dependence can be used as an instrumental function because Au NP is optically isotropic.

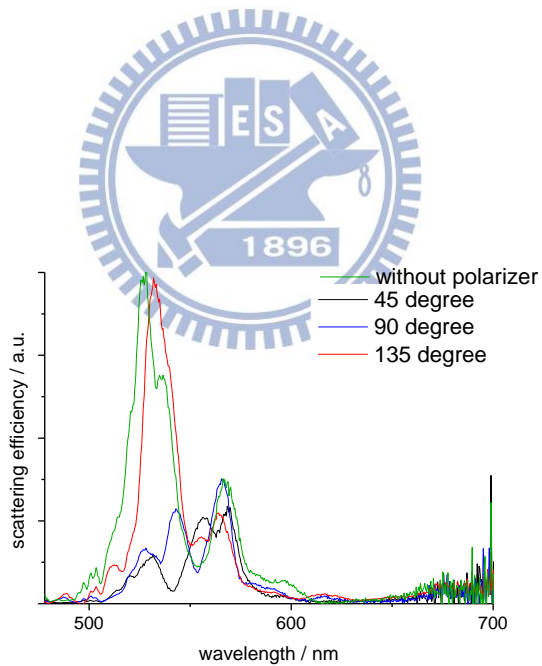


Fig. 4.18 Scattering spectra of granum without polarization and with 45, 90 and 135 degree.

The spectrum changed as the polarization changed, especially at the Soret band.

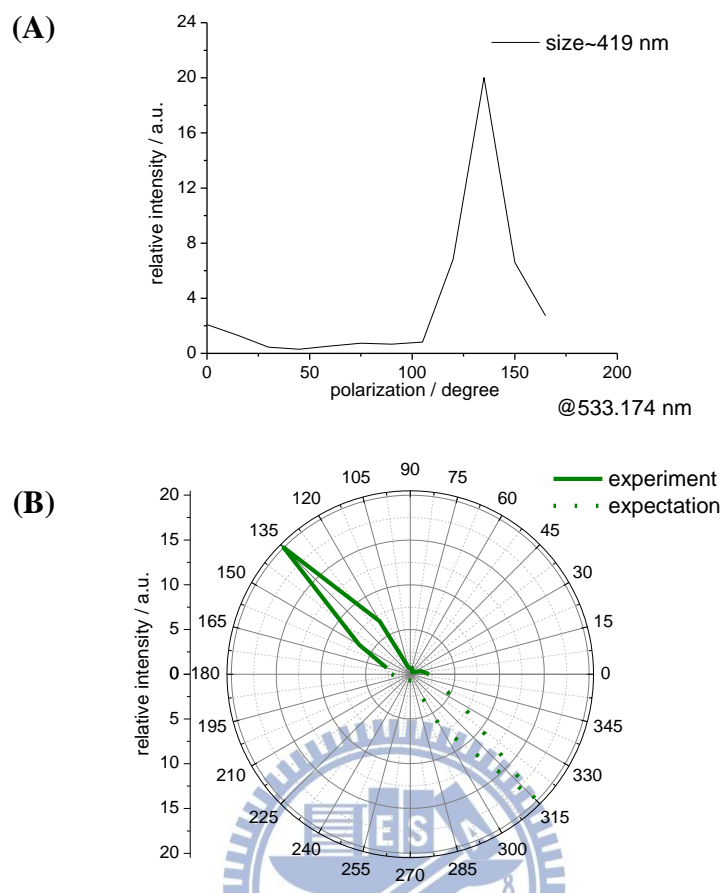


Fig. 4.19 Polarization dependence of granum. (A) The intensity of each angle was chosen from the scattering efficiency of each spectrum at 533 nm which had the maximum efficiency of the Soret band. The polarization plot then is corrected by instrumental function, and finally the polarization dependence was plotted. The polarization dependence indicated granum is optically anisotropic. (B) Polarization dependence expressed in polar coordinate system. The solid line is the experimental result and the dotted line is the expectation. The symmetry was expected since we used linear polarization.

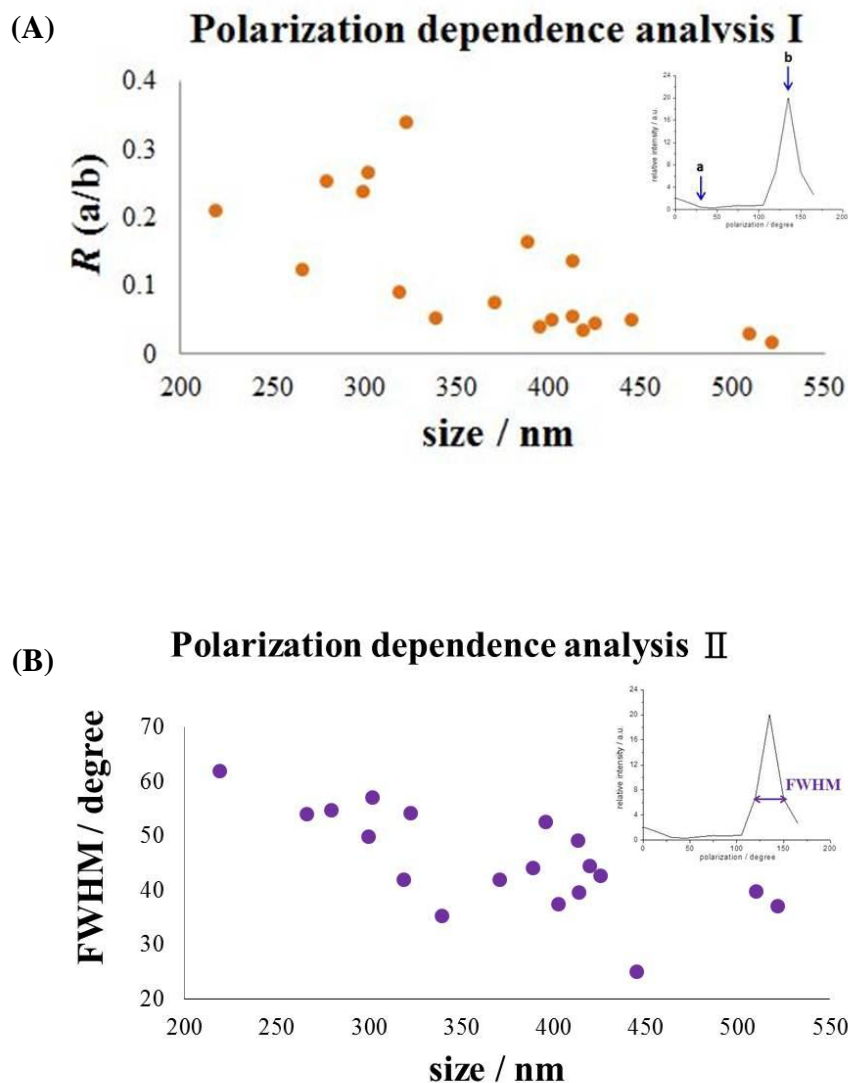
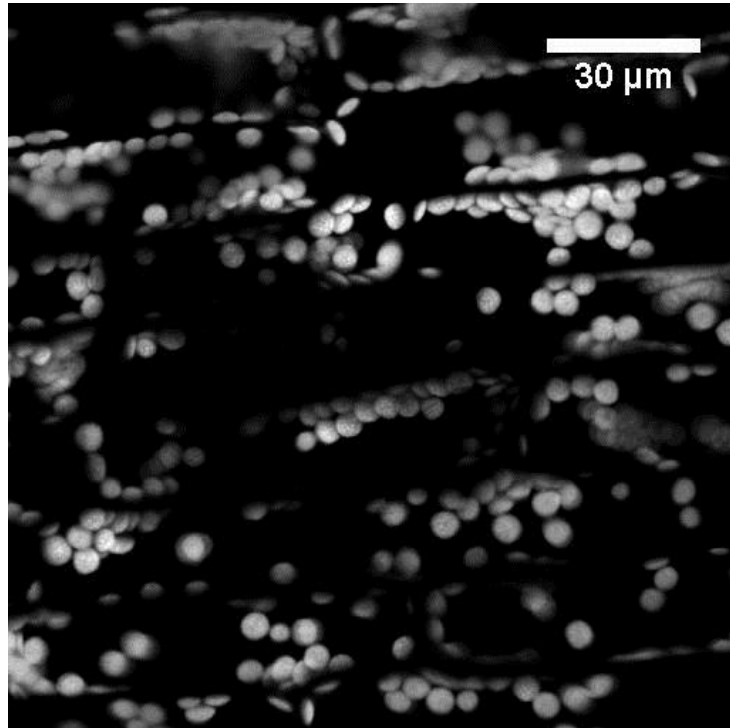


Fig. 4.20 The analyses of polarization dependence. (A) R is defined by the ratio of the minimum and maximum the values of the polarization dependence. The inset illustrated the parameters of R . It is clear that R decreases as size of granum enlarges. (B) The y-axis stood for the FWHM shown in the inset. FWHM was calculated by Gaussian fit. In general, FWHM and the size represent negative correlation.

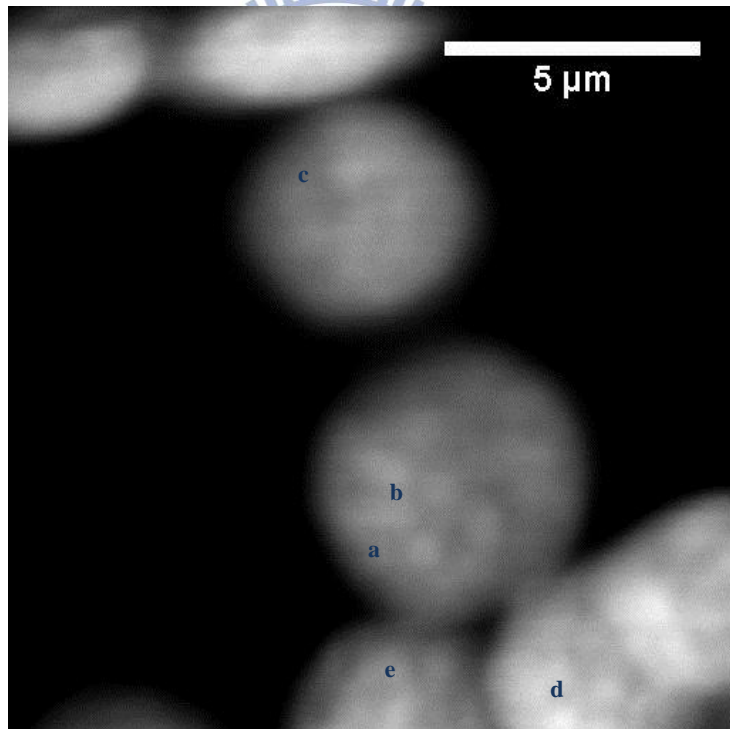
Chlorophyll fluorescence analysis has become one of the most powerful and widely used techniques, which is available to plant physiologists and ecophysiologicalists [31]. In this study, we also apply fluorescence measurement to living grana. Sample was directly excited by 488 nm Ar-ion laser. This means that the shoulder of Soret band is excited. Although the total fluorescence yield of chlorophyll is very small (only 1 or 2% of total light absorbed), measurement is quite easy because of strong fluorescence intensity due to high fluorescence cross section [31]. Fig. 4.21 (A) and (B) are the fluorescence images with one and ten times zooming respectively. Compared to Fig. 4.4, only chloroplasts were observed and their cell wall was not depicted directly, but it could be distinguished from the distribution of chloroplast. In addition, the 3-D spatial distribution can be differentiated from the brightness of chloroplast. By contrast with Fig. 4.6, the fluorescence image showed lower resolution, only few and unclear grana could be recognized. In contrast to 90 grana observed on average in one chloroplast from the CLSM image, less than 20 grana are clearly observed in the fluorescence image. On the other hand, the granal size of fluorescence image is around 600 nm which is almost 2 to 3 times larger than that of CLSM image. It implies that a granum in the fluorescence image may contain 2 to 3 grana. These demonstrated that CLSM is better than fluorescence measurement in living cell.

Chlorophyll fluorescence emission spectra were measured from various sites of the imaged chloroplasts. Results are shown in Fig. 4.21 (C) and (D), with the spectra normalized at 684 nm. Spectra a and b show grana in the same chloroplast, spectra a, c, d and e illustrate the spectral shapes of grana from different chloroplasts. Obviously, the discrepancy among them is quite small. In other words, the fluorescence spectrum is independent on granum size and position in the chloroplast. The results suggest that (i) the grana contain different kinds of molecules with various relative intermolecular orientations and many of them play as a fluorescence quencher with different quenching efficiency, and (ii) some grana may undergo non-radiative decay. Hence, the signal-to-noise ratio of the light scattering is better than that of the fluorescence, so that the spatial resolution of light scattering is apparently better compared to the fluorescence imaging. The consequences indicate that, as compared to fluorescence measurement, light scattering measurement is more suitable for *in vivo* grana to obtain information about the size and anisotropic structure.

(A)



(B)



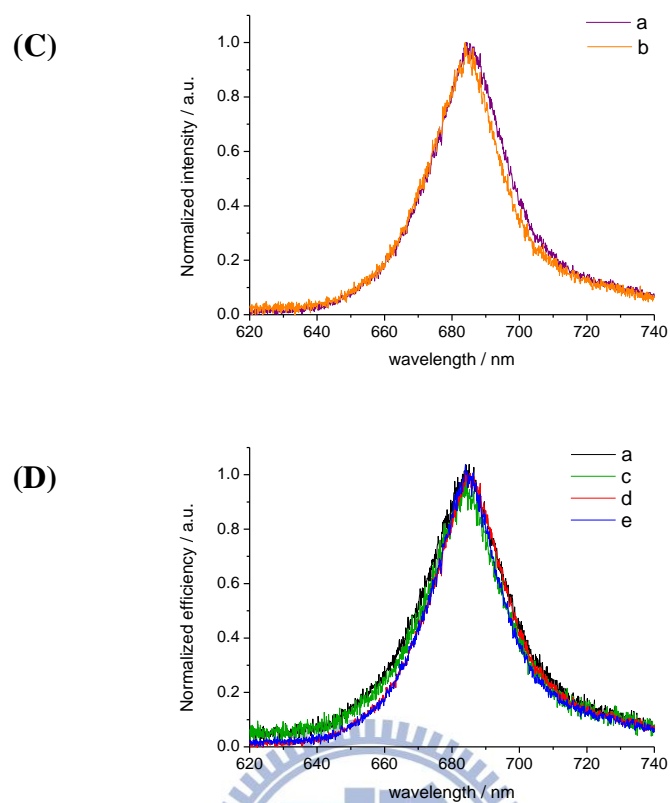


Figure 4.21 Fluorescence images and spectra are shown. (A) The fluorescence image of plant cell without magnification. Different brightness depicts the distance from the focal plane. (B) The fluorescence image of plant cell with 10 times magnification. Only some grana are recognized. (C) The fluorescence spectra of two grana in the same chloroplast. (D) The fluorescence spectra of grana in different chloroplast.

4.3 Discussion

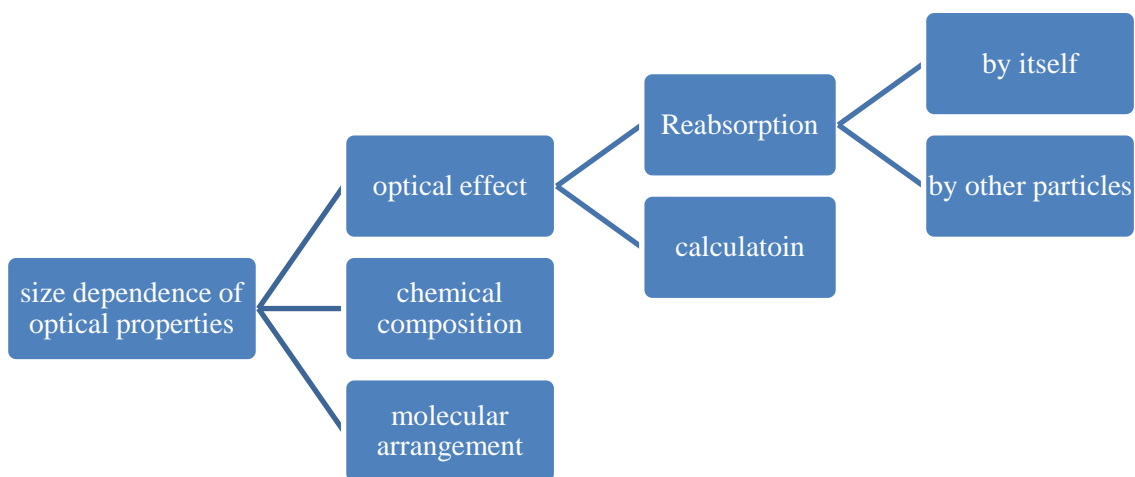
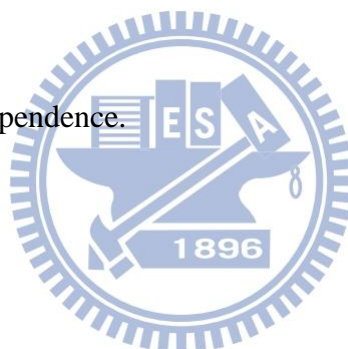


Fig. 4.22 The analysis of size dependence.



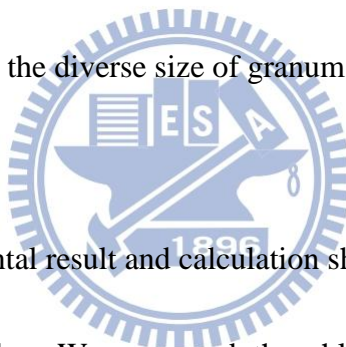
To interpret the granum size-dependence of the Soret band of the spectrum, first we should consider what important factors determine the Soret band. Size dependence of electronic spectra could be discussed based upon optical property. Here we list three possibilities that might be the effective factors of size dependence; **chemical composition**, **optical effect** and **molecular arrangement** (Fig. 4.22). The further detail of each element will be discussed in the following sections, which includes the computational calculation and experimental evidences.

When mentioning molecular electronic spectra, chemical composition of the species usually comes up. It is known that various pigments in the grana and their compositions differ for each granum. The fluctuation of chlorophyll *a* usually varies with different extracting procedures or solvents, but the main pigment composition is still chlorophyll *a* [33, 34]. This finding is not only limited to *E. densa* but also presented in other plants [35]. In other words, although the spectra vary slightly from granum to granum due to different composition, the primary shape should retain the same. Since the composition of granum only has minor influences on the spectrum, the factor of **chemical composition** can be excluded from the possibilities.



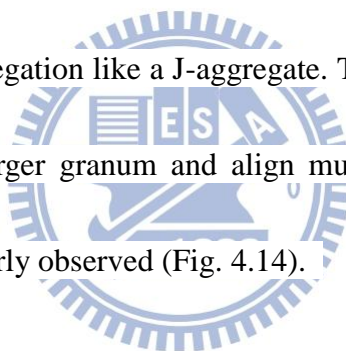
Optical effect can be divided into two parts, reabsorption and calculation. Reabsorption denotes that the scattered light from a sample is reabsorbed by surrounding or the sample itself. In this study, reabsorption means the scattered light from granum is reabsorbed by other grana or itself. Reabsorption by granum itself can be neglected because the grana are small enough (average size is 273 nm). In section 4.2-2, we have already proven the position dependence. Actually, the position dependence showed the indirect verification that reabsorption by other grana was very small. The spectra of grana in arbitrary site discriminating non-dissimilarities implied that the reabsorption effect was so unobvious that could be ignored.

Next, we used Mie theory to calculate the scattering efficiencies and optical resonance wavelengths of grana for various dimensions, so as to clarify the size dependence of grana. To simplify the calculation, we assumed that granum is a spherical NP full of chlorophyll *a* and the refractive index of surrounding media is homogeneous, equals to 1.33 for water. Fig. 4.23 shows the scattering spectra of the chlorophyll *a* NPs. Size dependences of experimental result and calculation are plotted in the Soret band of spectra against size in Fig. 4.24 and the inconsistency is clearly depicted. Experimental result revealed positive correlation between size and spectrum, while calculation presented size independence, i.e. the spectral shift of the Soret band does not occur due to the diverse size of granum.



The gap between experimental result and calculation shown in Fig. 4.24 can be explained by the presumed refractive index. We supposed the chlorophyll *a* NPs are dispersed in solution. As a matter of fact, the surrounding media is more similar to solid since molecular pigments are embedded in the LHC bound to thylakoid membrane. Based on Mie theory, a red-shift would come in the optical spectra with larger refractive index of environment. If we had learned the real refractive index of granum, the gap would be much smaller than the result. Hence, **optical effect** can be excluded from the possible explanations.

The aggregation and dimerization of porphyrins and metalloporphyrins in aqueous solution have been widely described. As the natural chlorophyll aggregates in the light-harvesting proteins or chlorosomes have a strong transition dipole moment aligned in the “head-to-tail” direction, porphyrin J-aggregates are important for the study of the excited-state model of the organisms [36]. J-aggregate is a one-dimensional molecular arrangement in which the transition moments of individual monomers are aligned in parallel. The strong coupling of several self-similar monomers results in a coherent excitation at red-shifted wavelengths relative to the monomer [37]. The following inference is reasonable that chlorophyll pigments form aggregation like a J-aggregate. That is to say, we can consider that there are more molecules in larger granum and align much uniformly. As a consequence, redshift of optical spectra is clearly observed (Fig. 4.14).



Analyses of polarization dependence (Fig. 4.20) also support the above assumption. If the molecules align one-dimensionally perfectly, the interaction between irradiation and molecules should be strongly clear, i.e. the polarization plot (Fig. 4.19) would show a narrow peak at certain angle while others stay level. On the other hand, the narrower the FWHM is, the better molecules align. This is what parameter R stands for. Fig. 4.20 (A) indicates R decreases with respect to size, reflecting size dependence. Same meaning as Fig. 4.20 (B) represented. FWHM decreases against the increase of size.

All of the experimental results illustrate size dependence, and consequently we could confidently suggest that pigment arrangement changes depending on the size of granum.

Because the aggregation of chlorophyll leading to exciton generation are able to capture the incident light and transfer the energy to “reaction center” with higher efficiency compared to isolated condition, it can be considered that our finding suggests the inhomogeneity of chloroplast in view of light-harvesting.

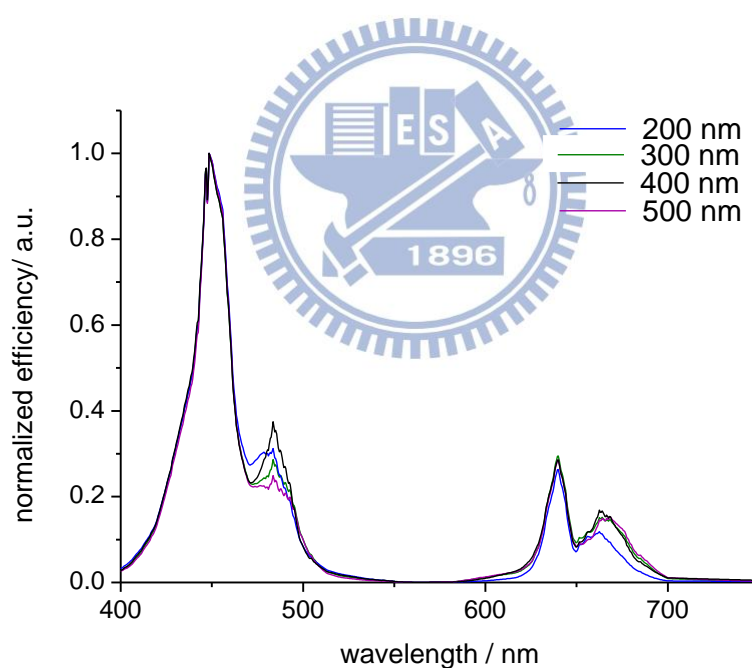


Figure 4.23 The calculation of chlorophyll *a* NP. Calculating scattering spectrum of granum which contains lots of chlorophyll pigments is complicated, so we calculated chlorophyll *a*, the main component of granum instead. Based on Mie theory, calculated scattering spectra of chlorophyll *a* NPs, from 200 nm to 500 nm, were obtained.

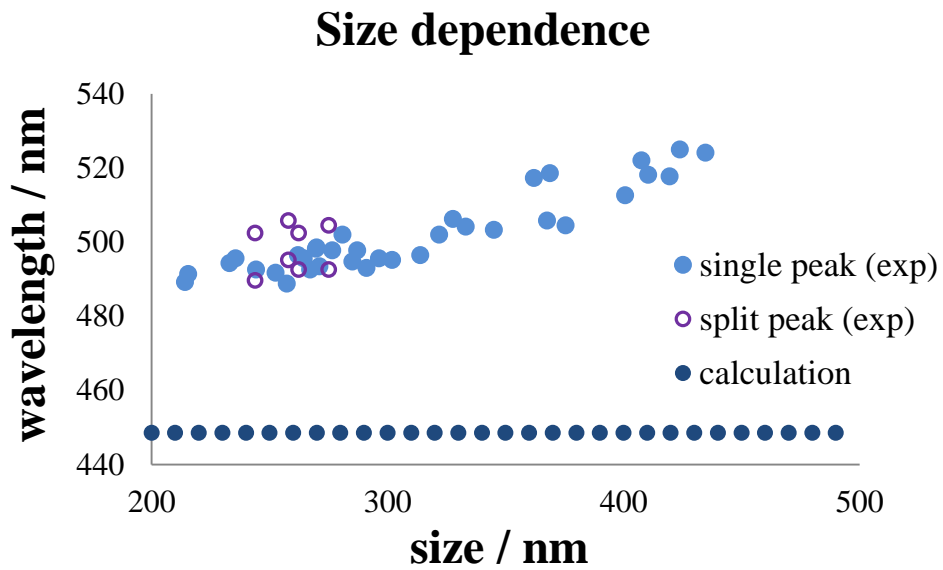


Figure 4.24 The plot of peak wavelength of the Soret band against size. The plot showed size dependence of experimental result and calculation. Calculation represented size independence and the Soret band located at around 450 nm differing from experimental result. The difference between the Soret band of experimental result and calculation is contributed to the refractive index of media. Chlorophyll pigments embedded in protein bound to membrane, so the environmental area can be considered as solid, while we assumed water as media. Redshift presents when the environmental refractive index increases.

4.4 Summary

We have successfully demonstrated *in vivo* and high spatial resolution spectroscopic study on chloroplast in plant cell by using confocal Rayleigh scattering microspectroscopic imaging system.

By confocal microscope, the detection volume is confined to extremely small. Besides, the supercontinuum improves the spatial resolution down to 250 nm. Confocal Rayleigh scattering microspectroscopic imaging system could measure submicron-sized particles; moreover, only this system can obtain the spectral information of single organelle *in vivo*.

Light scattering spectra of grana differ from each granum, and we found the correlation exists between spectrum and size of granum. Polarization experiment indicates that granum is optical anisotropy and implies that chlorophyll pigments form J-aggregate like, and the arrangement tends to be longer in larger granum. It is also implies that larger grana possess higher efficiency of photosynthesis.

Chapter 5 Three dimensional spectroscopic

characterizations of glycine crystals incorporated with Au NPs

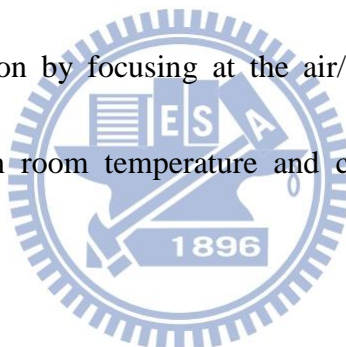
We have detected single granum in vivo, submicron particle in the plant cell, by confocal light scattering microspectroscopy and imaging system. In order to ensure **the reliability of the result**, we imitated an artificial complex system with corresponding natural complex system. The artificial complex system was prepared by Au NPs incorporated in glycine crystal. Au NPs have been widely used and have been optically characterized well, so they are the best material as standard. Glycine is the smallest amino acid whose three types of crystal polymorphs are α , β , and γ -form. Since α -polymorph is dynamically the most stable polymorph, it is easier to obtain and also mainly used in this work.

5.1 Sample preparation

Glycine (99.0%, Lot. No. LTf4344, Wako Pure Chemical) in the form of white powder was used without any purification. Considering the probability of Au NPs being embedded in the crystal, we used 40 nm Au colloidal solution (British Biocell). Deionized water, as a solvent, was filtered with a syringe filter (pore size; 0.22 μ m, SLGV 013 SL, Millipore) before dissolving glycine. 4 mL blood vial (BERSING TECHNOLOGY CO., LTD) was used as container for easy removing the unattached crystals from bottle. 1.3 supersaturation degree of

glycine aqueous solution was prepared by mixing 0.21 g glycine powder, 0.15 mL 40 nm Au colloidal solution and 0.45 mL deionized water into vial with cap screwed on. The solution was slowly heated up from room temperature to 60°C in water bath for 10 hours. The temperature was cooled down to room temperature 7°C per hour when glycine was totally dissolved.

According to the previous study [25], we used amplified fs laser (wavelength; 800 nm, pulse duration; 160 fs, pulse energy; 100mW, repetition rate; 1000 Hz, exposure time; 10 minutes) to induce crystallization by focusing at the air/solution interface (Fig. 5.1). The experiments were performed in room temperature and crystals were observed within 10 minutes (Fig. 5.2).



For microscopic characterization, we used a chamber to place some crystal with a glass substrate as base, immersion oil to decrease reflection and another glass substrate as cover (Fig. 5.3).

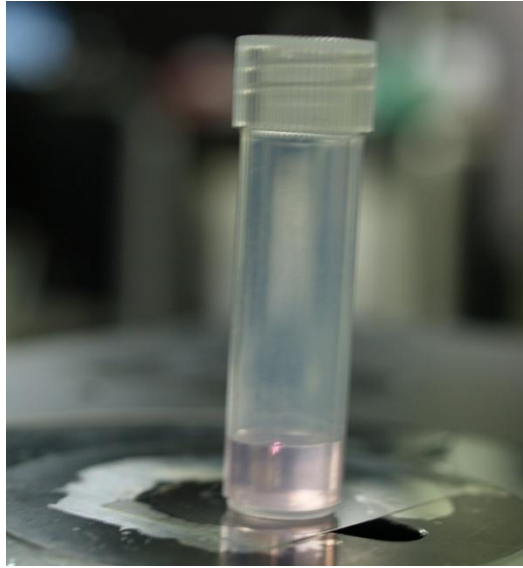


Figure 5.1 We focused fs laser at the air/ solution interface to induce crystallization.

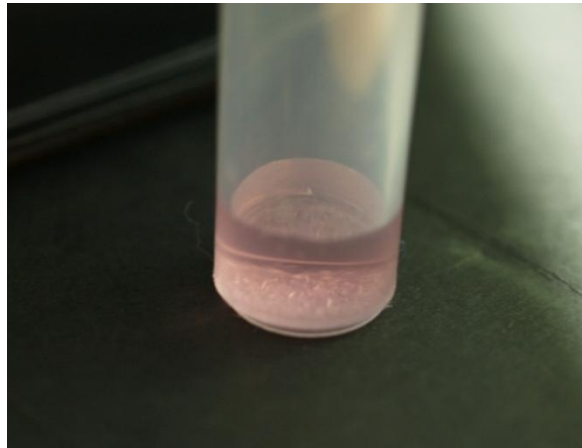


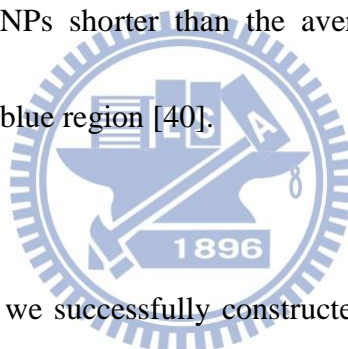
Figure 5.2 We can obtain many small crystals after irradiation.



Figure 5.3 Several glycine crystals were put into the chamber with immersion oil.

5.2 Results

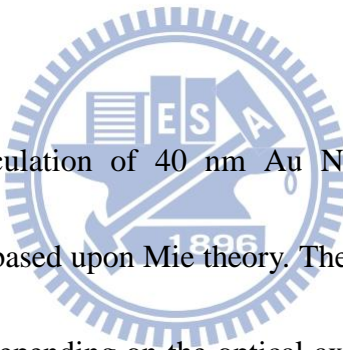
Figure 5.4 shows the picture of glycine crystal incorporated Au NPs. Due to diffraction limit and reflection by complicated structure of crystal, Au NPs presented various colors which changed slightly at altered depth. The colors of the scattered light also might correspond to the assorted sizes of aggregated Au NPs, for instance, in suspension solution, green is ca. 30-50 nm diameter, yellow is ca. 60-80 nm, and red is ca. 100 nm or larger according to the Mie theory of light scattering [38, 39]. When Au NPs aggregated leading to the distance between two Au NPs shorter than the average size of individual NP, their plasmon band will appear in the blue region [40].



With the help of software, we successfully constructed 3-D tomography by orthogonal views (Fig. 5.5). In XY-view, we can observe many bright spots related to locations of Au NPs and the reflection from the crystal by comparing the picture of crystal (Fig. 5.6). Au NPs were dispersed arbitrarily, some were localized (blue arrow) and some were separated. The yellow circles in XZ-view indicated that Au NPs were deeply embedded in the glycine crystal.

We have modeled a complex system, which was confirmed by confocal images depicting that Au NPs were inside crystal, not on the surface. Fig. 5.7 illustrates the light scattering spectra of Au NPs embedded in the glycine crystal. Among the spectroscopic result, we can

find not only the isolated Au NPs but also aggregated ones. The *localized surface plasmon resonance (LSPR)* band shifted owing to the particle size or shape of Au NPs. Most of the scattering spectra represented aggregated results that the LSPR band was in near IR region (Fig.5.7 (A)). Fig.5.7 (B) shows two bands in consequence of Au NP dimer, which is explained by electromagnetic interaction between two dipoles of each LSPR bands [40]. In contrast, Fig. 5.7 (C) shows one band assigned to a single particle. As shown here, simultaneous spectroscopic analysis with imaging helps us to distinguish isolated Au NPs from aggregated ones.



The red curve is the calculation of 40 nm Au NPs in the factor of 1.58 of the environmental refractive index, based upon Mie theory. The refractive index of α -form crystal ranges between 1.49 and 1.67, depending on the optical axes [41]. The consistence indicated that our measurement is accurate; as a result, the measurements of grana in the chloroplast are reliable.

Primarily we prepared glycine crystals hybridizing Au NPs by spontaneously crystallization with 1.4 supersaturation degree of glycine aqueous solution. Under this condition, we almost obtained γ -polymorph of glycine since γ -form is thermodynamically stable. All Au NPs were really loaded in and concentrated at the edge, so crystal presented

colorful; transparent to pink from center to the edge of the crystal (Fig. 5.8). Pink crystal suggested that Au NPs were aggregated and hard to find isolated one.

Fig. 5.6 and Fig. 5.8 revealed that fs laser is a better way to prepare the ideal complex system, i.e. α -polymorph glycine crystal incorporated Au NPs. In addition, we can use fs laser to tune the size of the crystal and control the place where nucleation occurred [25].



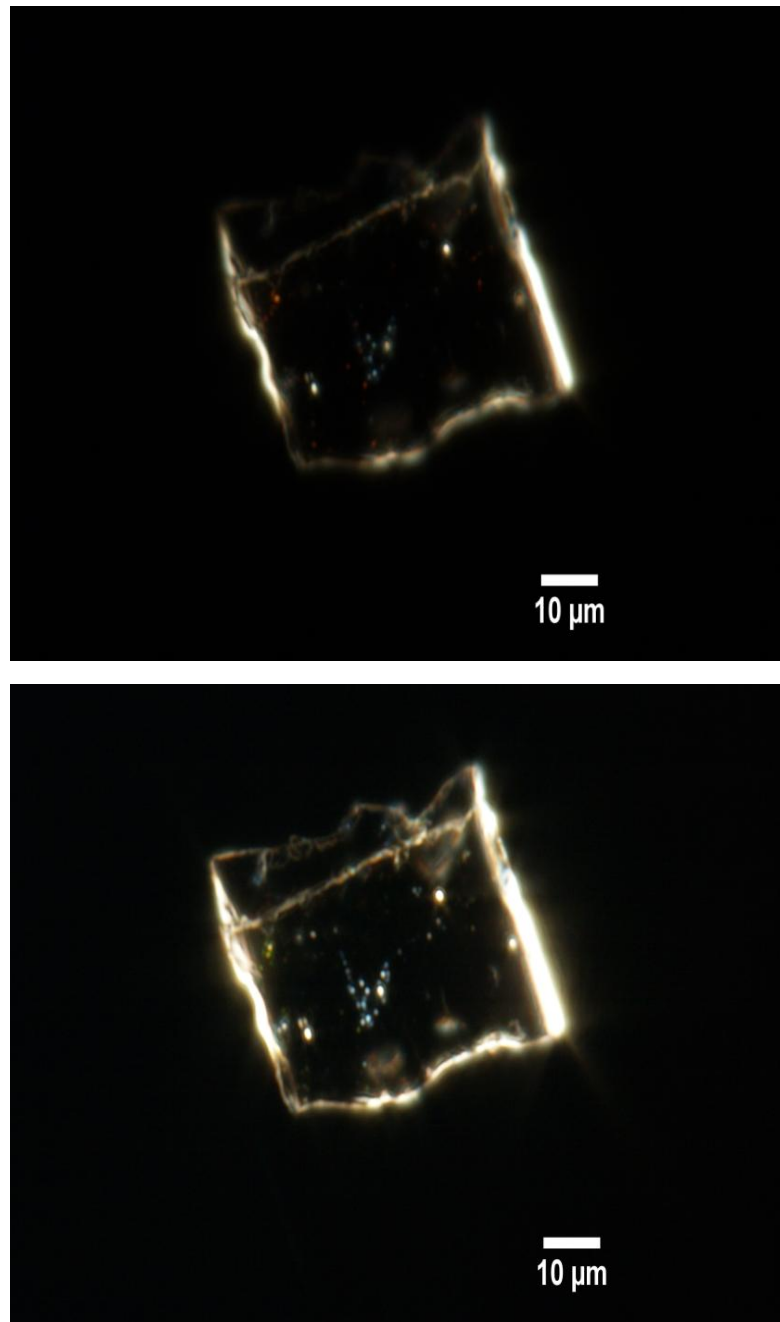


Figure 5.4 The pictures of glycine crystal incorporated Au NPs. Same crystal and same light intensity, the only difference is the height of the X-Y plane. With the various heights, Au NPs presented diverse colors, while the white spots would be attributed to crystal defects.

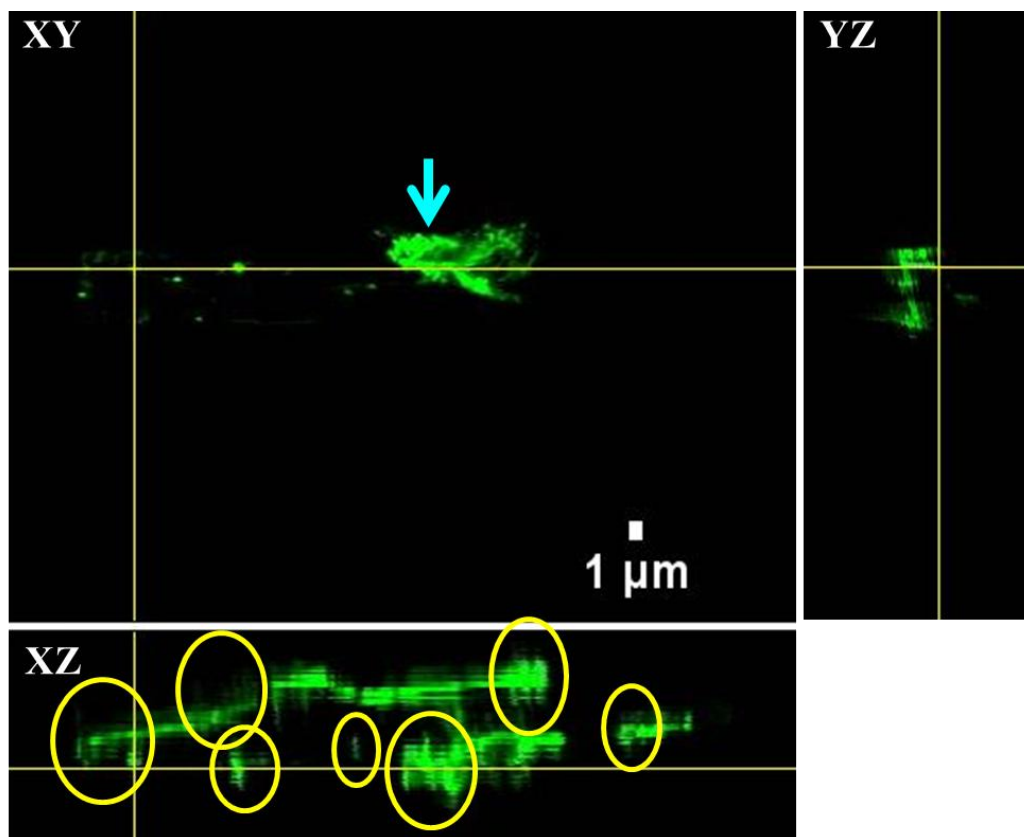


Figure 5.5 The tomography of glycine crystal. In XY-view, we can clearly see the localized Au NPs and the isolated Au NPs. The yellow circles in XZ-view pointed out that Au NPs were inside the crystal.

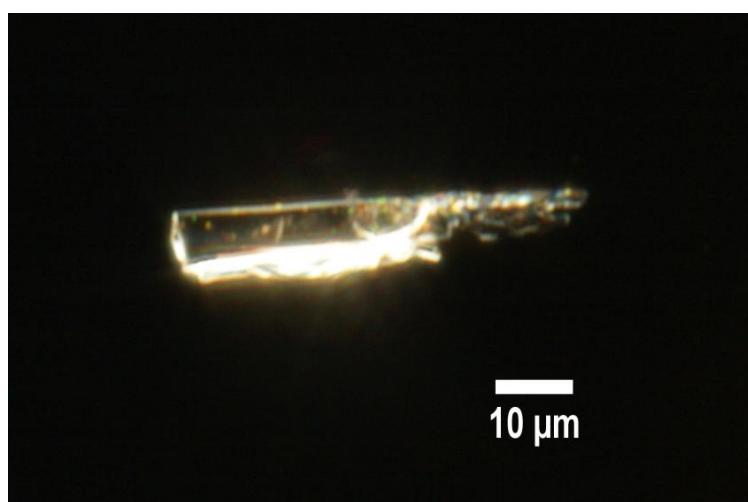


Figure 5.6 The picture of glycine crystal corresponding to the confocal image of X-Y plane in Fig. 5.5.

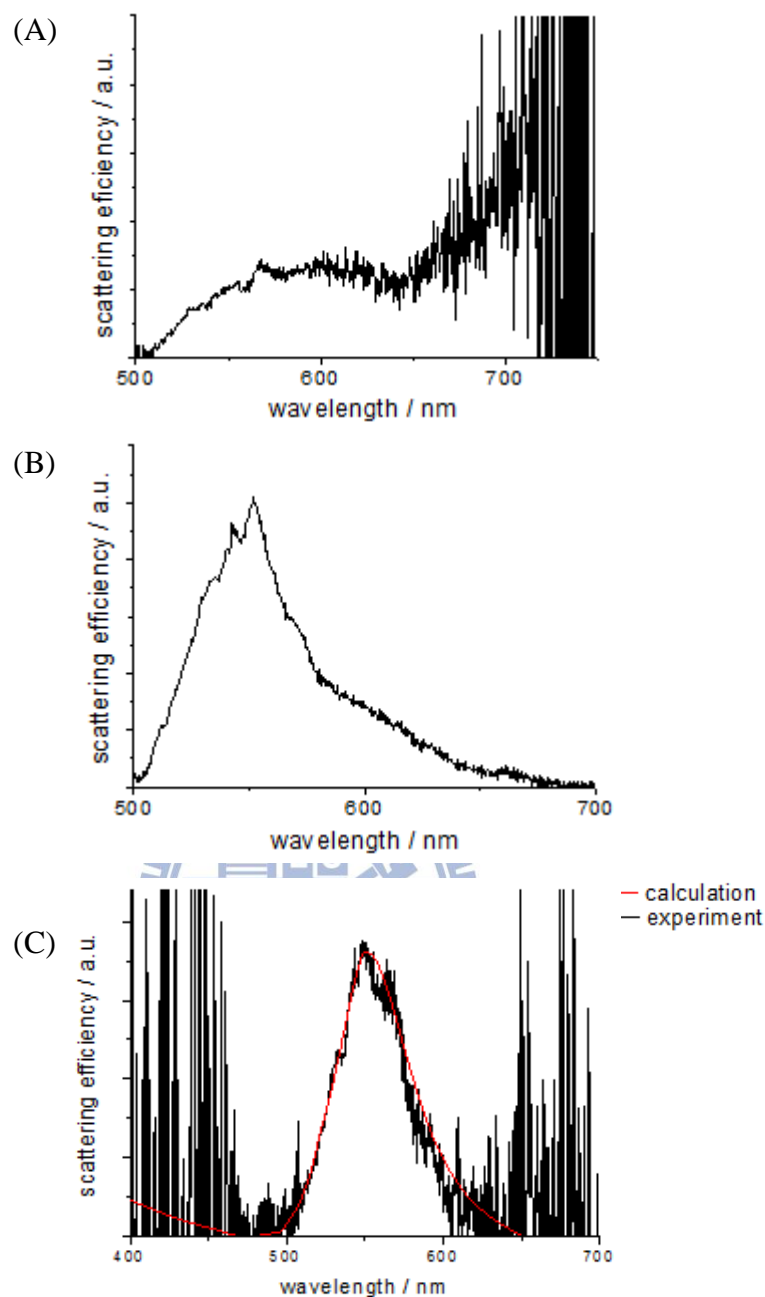


Figure 5.7 Light scattering spectra of Au NPs doped in α -polymorph glycine crystal. (A) Light scattering spectrum of aggregated Au NPs so that the band showed in near IR region. (B) The shoulder of the spectrum might be owing to Au NP dimer. (C) Light scattering spectrum of 40 nm Au NP (black curve). Red curve is the computational calculation of 40 nm Au NPs in the media which the refractive index is estimated as 1.58, the median of refractive index of α -form glycine crystal [41].

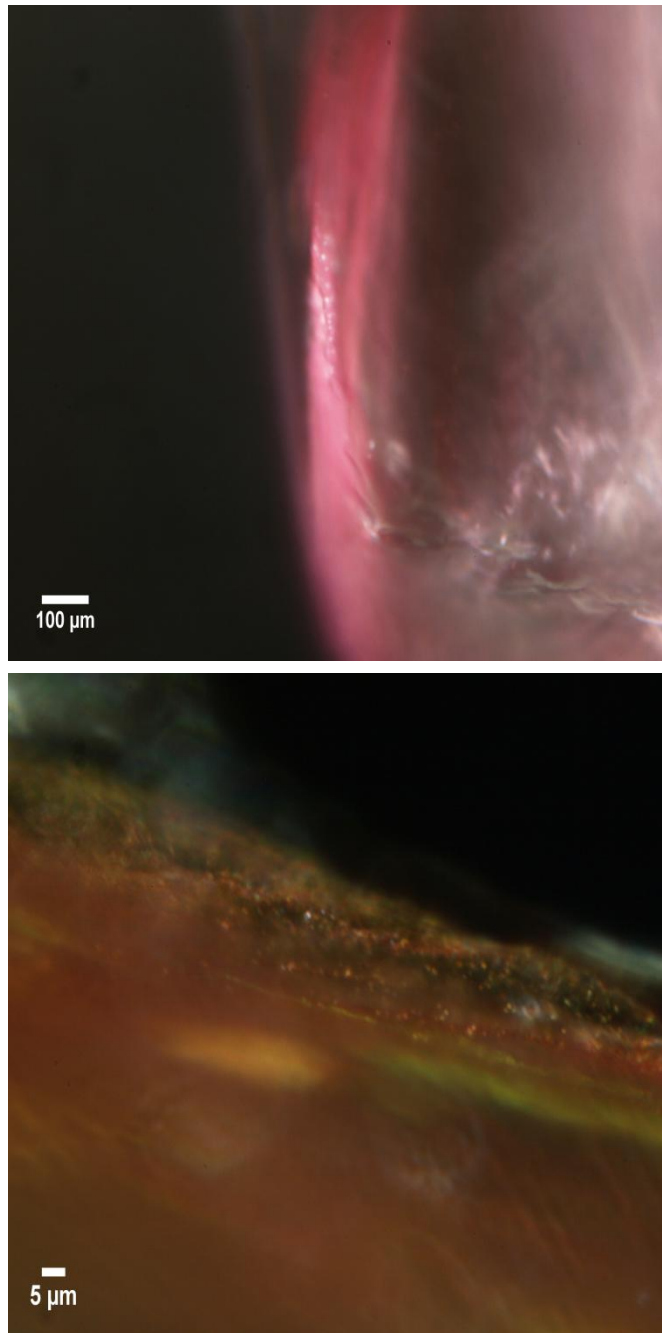


Figure 5.8 The pictures of γ -form glycine crystal. In upper picture, we can observe pink at the edge while others remained light pink. The below picture showed Au NPs concentrated at the edge.

5.3 Summary

In this study, we proved the reliability of the results of grana indirectly by measuring Au NPs embedded in the α -polymorph glycine crystal. Besides, the measurement of 40 nm Au NPs also showed the advantage of confocal Rayleigh scattering microspectroscopy and imaging system.



Chapter 6 Conclusion

In this study, we explored the inhomogeneity of grana of *Egeria densa* by confocal Rayleigh scattering microspectroscopy and imaging system. Confocal images showed the spatial distribution of grana which were distributed randomly. And the average size of granum is around 273 nm. With the help of pinhole, we can measure the light scattering spectrum of single granum. The light scattering spectra of grana differed from particle to particle. We also found that the spectra were independent on the positions of grana, either they are in the center or on the exterior of the chloroplast. Moreover, the greatest finding is the size dependence of granum; the Soret band of the spectra of grana shifted to longer wavelength with the increasing granum size. Polarization measurement indicated that grana are optically anisotropic. According to the analyses of results, it is considered that there are more chlorophyll pigments in larger granum and the molecules align much better in larger ones when irradiated by laser. Based on the inference, we suppose that the light-harvesting property of grana is reflected in size. Only our system can obtain the result of size dependence by measuring *in vivo* single granum in the chloroplast.

The experiment of “three dimensional spectroscopic characterization of glycine crystals incorporated with Au NPs” is used to prove the reliability of the spectroscopic data of grana.

Though 40 nm is much smaller than the resolution and Au NPs are embedded in crystal, we still can measure the light scattering spectra correctly. This provided indirect evidence that the measurements of grana were dependable. Besides, it also showed the superiority of confocal light scattering microspectroscopy.

To sum up, the present result reveals confocal Rayleigh scattering microspectroscopy and imaging system is capable for visualizing nanoparticles confined in the complicated medium, allowing *in situ* observation in the absence of fluorophores.



Reference

1. M. W. Davidson and M. Abramowitz, *Optical Microscopy*, Olympus America Inc., Melville, New York, USA (1999)
2. Van Dijk M A, Tchebotareva A L, Orrit M, Lippitz M, Berciaud S, Lasne D, Cognet L and Lounis B, *Absorption and scattering microscopy of single metal nanoparticles*, Phys. Chem. Chem. Phys. 8, 3486 (2006)
3. S. Berciaud, L. Cognet, G. A. Blab, and B. Lounis, *Photothermal Heterodyne Imaging of Individual Nonfluorescent Nanoclusters and Nanocrystals*, Phys Rev Lett 93, 257402 (2004).
4. R. H. Webb, *Confocal optical microscopy*, Rep. Prog. Phys. 59, 427-471 (1996).
5. W. Denk, J. H. Strickley, and W. W. Webb, *Two-photon laser scanning fluorescence microscopy*, Science 248, 73W (1990)
6. Brakenhoff, G.J., Squier, J., Norris, T., Bliton, A.C., Wade, M.H., Athey, B., *Real-time two-photon confocal microscopy using a femtosecond, amplified Ti: sapphire system*, J. Microsc. 181, 253 (1996)
7. Dunsby, C., Lanigan, P.M.P., McGinty, J., Elson, D.S., Requejo-Isidro, J., Munro, I., Galletly, N., McCann, F., Treanor, B., Ö nfet, B., Davis, D.M., Neil, M.A.A., and French, P.M.W., *An electronically tunable ultrafast laser source applied to fluorescence imaging and fluorescence lifetime imaging microscopy*, J. Phys. D: Appl.Phys. 37, 3296 (2004)
8. C.F. Kaminski, R.S. Watt, A.D. Elder, J.H. Frank, J. Hult, *Supercontinuum radiation for applications in chemical sensing and microscopy*, Appl. Phys. B, 92, 367 (2008)
9. Selci, S., Bertani, FR., Ferrari, L, *Supercontinuum ultra wide range confocal microscope for reflectance spectroscopy of living matter and material science surfaces*, AIP ADVANCES 1, 032143 (2011)
10. J. H. Frank, A. D. Elder, J. Swartling, A. R. Venkitaraman, A. D. Jeyasekharan, and C. F. Kaminski, *A white light confocal microscope for spectrally resolved multidimensional imaging*, J. Microsc. 227, 203 (2007).
11. Rajadhyaksha M., Grossman M., Esterowitz D., Webb R. H., Anderson R. R., *In vivo confocal scanning laser microscopy of human skin: melanin provides strong contrast*, J. Invest. Dermatol., 104, 946 (1995)
12. Korlach J, Schwille P, Webb WW, Feigenson GW, *Characterization of lipid bilayer phases by confocal microscopy and fluorescence correlation spectroscopy*, Proc Natl Acad Sci USA ,96, 8461 (1999)
13. R. Mercatelli, S. Soria, G. Molesini, F. Bianco, G. Righini, F. Quercioli, *Supercontinuum source tuned by an on-axis monochromator for fluorescence lifetime imaging*, Opt Express, 18, 20505 (2010)

14. Lindfors, K.; Kalkbrenner, T.; Stoller, P.; Sandoghdar, V., *Detection and Spectroscopy of Gold Nanoparticles Using Supercontinuum White Light Confocal Microscopy*, Phys. Rev. Lett., 93(3), 037401 (2004)
15. Louit G, Asahi T, Tanaka G, Uwada T, Masuhara H., *Spectral and 3-dimensional tracking of single gold nanoparticles in living cells studied by Rayleigh light scattering microscopy*, J Phys Chem C., 113, 11766 (2009)
16. J.P. Dekker, E.J. Boekema, *Supramolecular organization of the thylakoid membrane proteins in green plants*, Biochim. Biophys. Acta, 1706, 12 (2005)
17. Liu, Z. *et al.*, *Crystal structure of spinach major light-harvesting complex at 2.72 Å resolution*, Nature 428, 287 (2004)
18. L. Mustárdy, G. Garab, *Granum revisited. A three-dimensional model—where things fall into place*, Trends Plant Sci., 8, 117 (2003)
19. Mustárdy, L., Buttle, K., Steinbach, G., and Garab, G., *Three-dimensional architecture of the granum-stroma thylakoid membrane system revealed by electron tomography*, In Energy from the Sun: 14th International Congress on Photosynthesis, J.F. Allen, E. Gantt, J.H. Golbeck, and B. Osmond, eds (Heidelberg, Germany: Springer), 771 (2008)
20. Bohren C.F., Huffman D.R., *Absorption and scattering of light by small particles*, Wiley: New York (1998)
21. Yeh CH, Chow CW, Sung JY, Wu PC, Whang WT, Tseng FG, *Measurement of organic chemical refractive indexes using an optical time-domain reflectometer*, Sensors, 12, 481 (2012)
22. Willets, K. A. & Van Duyne, R. P., *Localized surface plasmon resonance spectroscopy and sensing*, Annu. Rev. Phys. Chem. 58, 267 (2007)
23. I. W. Sudiarta and P. Chylek, *Mie-scattering formalism for spherical particles embedded in an absorbing medium*, J. Opt. Soc. Am. A 18, 1275 (2001)
24. I. W. Sudiarta and P. Chylek, *Mie scattering efficiency of a large spherical particle embedded in an absorbing medium*, J. Quant. Spectrosc. Radiat. Transfer 70, 709 (2001)
25. T. H. Liu, Master Thesis, National Chiao Tung University (2011)
26. M. D. Curt, G. Curt, P. L. Aguado and J. Fernandez, *Proposal for the Biological Control of Egeria densa in Small Reservoirs: A Spanish Case Study*, J. Aquat. Plant Manage. 48, 124 (2007)
27. Zumbusch, A., Holtom, G. R. & Xie, X. S., *Three-dimensional vibrational imaging by coherent anti-Stokes Raman scattering*, Phys. Rev. Lett. 82, 4142 (1999)
28. Olson, R. A., Jennings, W. H., and Butler, W. L., *Molecular orientation: Spectral dependence of dichroism of chloroplasts in vivo*, Biochim. Biophys. Acta 88, 318 (1964)
29. Finzi, L., Bustamante, C., Garab, G., & Juang, C.-B., *Direct observation of large chiral domains in chloroplast thylakoid membranes by differential polarization microscopy*, Proc. Natl. Acad. Sci. U.S.A. 86, 8748 (1989)
30. M. Ruosch, D. Marti, P. Stoller, J. Rička, and M. Frenz, *Dependence of the multiphoton*

- luminescence spectrum of single gold nanoparticles on the refractive index of the surrounding medium*, Proc. SPIE 7032 (2008)
31. Maxwell, K. & Johnson, G. N., *Chlorophyll fluorescence – a practical guide*, J. Exp. Bot. 51, 659 (2000)
 32. Shimoni, E., Rav-Hon, O., Ohad, I., Brumfeld, V., and Reich, Z., *Three-dimensional organization of higher-plant chloroplast thylakoid membranes revealed by electron tomography*, Plant Cell 17, 2580 (2005)
 33. Su, S.Q., Zhou, Y.M., Qin, J.G., Yao, W.Z., & Ma, Z.H., *Optimization of the method for chlorophyll extraction in aquatic plants*, J. Freshwat. Ecol., 25, 531 (2011)
 34. Casaty P., Lara M.V., Andreo C.S., *Regulation of enzymes involved in C4 photosynthesis and the antioxidant metabolism by UV-B radiation in Egeria densa, a submersed aquatic species*, Photosynthesis Res., 71, 251 (2002)
 35. Pagliano C., Raviolo M., Dalla Vecchia F., Gabbrielli R., Gonnelli C., Rascio N., Barbato R. & La Rocca N., *Evidence for PSII donor-side damage and photoinhibition induced by cadmium treatment on rice (Oryza sativa L.)*, J. Photochem. Photobiol. B: Biol. 84, 70 (2006)
 36. Okada, S., Segawa, H., *Substituent-Control Exciton in J-Aggregates of Protonated Water-Insoluble Porphyrins*, J. Am. Chem. Soc., 125, 2792 (2003)
 37. Maiti, N. C.; Mazumdar, S.; Periasamy, N., *J- and H-Aggregates of Porphyrin–Surfactant Complexes: Time-Resolved Fluorescence and Other Spectroscopic Studies*, J. Phys. Chem. B, 102, 1528 (1998)
 38. Yguerabide, J., Yguerabide, E.E., *Light-scattering submicroscopic particles as highly fluorescent analogs and their use as tracer labels in clinical and biological applications*, Anal. Biochem. 262, 157 (1998)
 39. S. Hashimoto, T. Uwada, H. Masuhara, T. Asahi, *Fabrication of Gold Nanoparticle-Doped Zeolite L Crystals and Characterization by Optical Microscopy: Laser Ablation- and Crystallization Inclusion-Based Approach*, J. Phys. Chem. C, 112, 15089 (2008)
 40. C. Y. Tsai, Master Thesis, National Chen Kung University (2005)
 41. Orttung, W. H.; Armour, R. W., *Polarizability Anisotropy from Crystal Refractive Indices. I. Lorentz Internal Field Approximation with Application to Amino Acid Datal*, J. Phys. Chem., 71, 2846 (1967)